

# AMERICAN METEOROLOGICAL SOCIETY

*Journal of the Atmospheric Sciences*

## **EARLY ONLINE RELEASE**

This is a preliminary PDF of the author-produced manuscript that has been peer-reviewed and accepted for publication. Since it is being posted so soon after acceptance, it has not yet been copyedited, formatted, or processed by AMS Publications. This preliminary version of the manuscript may be downloaded, distributed, and cited, but please be aware that there will be visual differences and possibly some content differences between this version and the final published version.

The DOI for this manuscript is doi: 10.1175/JAS-D-18-0146.1

The final published version of this manuscript will replace the preliminary version at the above DOI once it is available.

If you would like to cite this EOR in a separate work, please use the following full citation:

Akinlabi, E., M. Wacławczyk, J. Mellado, and S. Malinowski, 2019: Estimating turbulence kinetic energy dissipation rates in numerically simulated stratocumulus cloud-top mixing layer: evaluation of different methods. *J. Atmos. Sci.* doi:10.1175/JAS-D-18-0146.1, in press.

© 2019 American Meteorological Society



# **Estimating turbulence kinetic energy dissipation rates in numerically simulated stratocumulus cloud-top mixing layer: evaluation of different methods.**

Emmanuel O. Akinlabi<sup>1</sup>, Marta Waclawczyk<sup>1,\*</sup>

Juan Pedro Mellado<sup>2</sup> and Szymon P. Malinowski<sup>1</sup>

<sup>1</sup>*Institute of Geophysics, Faculty of Physics, University of Warsaw, Warsaw, Poland*

<sup>2</sup>*Max-Planck Institute for Meteorology, Hamburg, Germany*

<sup>\*</sup> *Corresponding author address:* Institute of Geophysics, Faculty of Physics, University of Warsaw,  
Warsaw, Poland.

E-mail: marta.waclawczyk@igf.fuw.edu.pl

## ABSTRACT

11 In this work, Direct Numerical Simulation (DNS) of stratocumulus cloud-  
12 top mixing layer is used to test various approaches to estimate the turbulence  
13 kinetic energy dissipation rate (TKE)  $\varepsilon$  from one-dimensional (1D) intersec-  
14 tions that resemble experimental series. Results of these estimates are com-  
15 pared with "true" (DNS) values of  $\varepsilon$  in buoyant and inhomogeneous atmo-  
16 spheric flows. We focus on recently proposed methods of the TKE dissipa-  
17 tion rate retrievals based on zero crossings and recovering missing part of the  
18 spectrum. These methods are tested on fully-resolved turbulence fields and  
19 compared to standard retrievals from power spectra and structure functions.  
20 Anisotropy of turbulence due to buoyancy is shown to influence retrievals  
21 based on vertical velocity component. TKE dissipation rate estimates from  
22 the number of crossings correspond well to spectral estimates. The method  
23 based on the recovery of the missing part of the spectrum works best for  
24 the Pope's model of dissipation spectrum and is sensitive to external inter-  
25 mittency. This allows for characterization of external intermittency by the  
26 Taylor-to-Liepmann scale ratio. Further improvements of this method are  
27 possible when the variance of the velocity derivative is used instead of the  
28 number of zero crossings per unit length. In conclusion, the new methods of  
29 TKE dissipation rate retrieval from 1D series provide a valuable complement  
30 to standard approaches.

## 31 1. Introduction

32 Turbulence contributes to many atmospheric phenomena, including atmospheric convection and  
33 clouds. An important quantity that characterizes the smallest scales of such flows is the mean  
34 turbulence kinetic energy (TKE) dissipation rate  $\varepsilon$ . In formulating sub-grid models for large eddy  
35 simulation (Moeng and Sullivan 1994; Patton et al. 1998) or Lagrangian trajectory analysis of  
36 passive scalars (Poggi and Katul 2006), a robust estimation of the TKE dissipation rate profile is  
37 needed.

38 Several methods have been proposed to calculate  $\varepsilon$  from 1D velocity time series by making use  
39 of the local isotropy assumption. Indirect methods are based on the inertial range arguments that  
40 follow from Kolmogorov’s hypotheses (Kolmogorov 1941; Albertson et al. 1997). Such methods  
41 are commonly used in the analysis of low- and moderate-resolution velocity time series of in-situ  
42 airborne measurements (Sharman et al. 2014; Kopeć et al. 2016a). In the case of fully-resolved  
43 velocity signals, the direct methods, based on measuring the mean variance of velocity fluctuation  
44 gradients, can be applied. Alternatively, Sreenivasan et al. (1983) proposed the zero-crossing ap-  
45 proach, which requires counting the number of times per unit length the velocity signal crosses  
46 the zero threshold, denoted by  $N_L$ , as shown in Figure 1. The so-called ‘Liepmann scale’ defined  
47 as  $\Lambda = 1/(\pi N_L)$ , is assumed to be equal to the transverse Taylor’s microscale  $\lambda_n$ , which is used to  
48 calculate  $\varepsilon$ . Since  $N_L$  in signals with spectral cut-off are much smaller than in fully resolved sig-  
49 nals, Waćławczyk et al. (2017) proposed two possible modifications to the zero-crossing method  
50 in order to estimate  $\varepsilon$  from moderate resolution measurement data.

51 The first method is based on a successive filtering of the velocity signal, assuming that turbulence  
52 is homogeneous, isotropic and that the inertial scaling of  $-5/3$  holds. In the second approach, an  
53 analytical model for the unresolved section of the spectrum is used to calculate a correcting factor

54 to  $N_L$ , so the actual relation between  $\varepsilon$  and  $N_L$  can be used. Waławczyk et al. (2017) validated  
55 these approaches on the data obtained during the Physics of Stratocumulus Top (POST) research  
56 campaign designed to investigate the marine stratocumulus clouds as well as the details of the  
57 vertical structure of the stratocumulus-topped boundary layer (Gerber et al. 2013; Malinowski  
58 et al. 2013).

59 The above-mentioned methods for  $\varepsilon$  retrieval are based on the local isotropy assumption. How-  
60 ever, this assumption might not always be fulfilled in real atmospheric conditions (Chamecki and  
61 Dias 2004; Jen-La Plante et al. 2016). Buoyancy is one reason for anisotropy in atmospheric flows.  
62 The energy spectra of buoyancy-driven turbulence has been studied by several authors (Bolgiano  
63 1959; Lumley 1964; Lindborg 2006; Waite 2011; Kumar et al. 2014). First Bolgiano (1959) and  
64 Obukhov (1959) proposed the energy spectrum should scale as  $E(k) \sim k^{-11/5}$  in stably stratified  
65 flows (referred to as BO scaling), where  $k$  is the wavenumber. Such scaling was later assumed  
66 to also hold in thermally-driven flows, however, a fine-resolution simulation performed by Kumar  
67 et al. (2014) revealed turbulent convection exhibit the Kolmogorov spectrum. This was also con-  
68 firmed by a DNS study of Rayleigh-Benard Convection (Verma et al. 2017) at  $Pr = \nu/\kappa \approx 1$ . Here,  
69  $\nu$  and  $\kappa$  are, respectively, the kinematic and thermal diffusivities of a fluid. Kimura and Herring  
70 (2012) investigated homogeneous incompressible turbulence, subjected to a range of degrees of  
71 stratification, using pseudo-spectral DNS method. The authors argued that due to the anisotropy  
72 of the flow a single mean dissipation rate cannot provide a universal Kolmogorov constant.

73 Physically complex atmospheric turbulence is not only inhomogeneous or buoyancy-driven,  
74 but also includes the co-existence of laminar and turbulent regions called external intermittency  
75 (Townsend 1956; Kurowski et al. 2009). The volume fraction occupied by a turbulent flow is  
76 called the intermittency factor  $\gamma$ . The motivation of this work is to investigate how the presence of  
77 anisotropy due to buoyancy and external intermittency affects the various retrieval techniques of

$\varepsilon$  in the atmospheric configurations, including the novel ones based on the number of crossings. Moreover, as the data used for the retrieval techniques are not idealized as DNS output, analysis of low-pass filtered velocity time series is undertaken, as measured by an artificial aircraft flying through the cloud, to assess performance of the methods. All the  $\varepsilon$ -estimates are compared with actual  $\varepsilon$  values from DNS of mixing layer at the stratocumulus cloud top. In spite of the inhomogeneity and physical complexity of the flow, the calculated  $\varepsilon$  profiles generally agree with DNS values within certain degree of accuracy. The observed deviations follow from the physical complexity of the flow and low-Re number of the DNS as compared to real atmospheric conditions. The latter issue makes the spectral retrieval methods difficult due to the relatively short inertial range. Further, an additional source of errors includes the deviations of the Taylor-to-Liepmann scale ratio from unity, as the assumption  $\lambda_n/\Lambda \approx 1$  lies behind the number of crossing method (Sreenivasan et al. 1983). In this work, we show that  $\lambda_n/\Lambda \approx \gamma$  in case of externally intermittent flows.

Due to the above-mentioned difficulties, the present work focuses on the second method proposed in Waclawczyk et al. (2017), based on an analytical model to resolving the missing part of the spectrum. We propose its alternative form, replacing the Liepmann scale, with the Taylor microscale. Results obtained with this new approach compare favourably with the DNS over a wide range of cut-off wavenumbers.

This paper is structured as follows: in section 2 we describe the current state of knowledge and propose modification of the iterative method. The set-up of the case study used in our analysis is explained in section 3. In sections 4 and 5 results of the TKE dissipation rate retrieval are presented. Section 6 provides a conclusion of the analysis results.

## 100 2. TKE dissipation rate estimates from 1D signals

### 101 a. Direct and indirect methods

102 The TKE dissipation rate is defined as (see e.g. Pope (2000))

$$\varepsilon = 2\nu \langle s_{ij}s_{ij} \rangle, \quad \text{where} \quad s_{ij} = \frac{1}{2} \left( \frac{\partial u'_i}{\partial x_j} + \frac{\partial u'_j}{\partial x_i} \right), \quad (1)$$

103  $s_{ij}$  is the fluctuating strain rate tensor,  $u'_i = u_i - \langle u_i \rangle$  denotes the  $i$ -th component of fluctuating ve-  
104 locity and  $\langle \cdot \rangle$  is the ensemble average operator. The exact definition cannot be used to estimate  $\varepsilon$  in  
105 case only 1D intersections of turbulent velocity field are available from experiments. Additionally,  
106 the resolution of the measured signals can be deteriorated due to finite sampling frequency of a  
107 sensor, as well as measurement errors.

108 The methods used to retrieve the TKE dissipation rate from 1D signals can be divided into two  
109 categories: direct and indirect. In direct methods the gradients of velocity are measured. Indirect  
110 methods relate the small-scale phenomenon of dissipation with inertial-range scales, as predicted  
111 by the second Kolmogorov's hypothesis (Kolmogorov 1941). Additionally, all methods are based  
112 on the local isotropy assumption (Kolmogorov 1941).

113 The two most common indirect approaches use an inertial-range scaling form of the power  
114 spectra and structure functions. In the homogeneous and isotropic turbulence, the following energy  
115 spectrum is assumed (Pope 2000)

$$E(k) = C\varepsilon_{PS}^{2/3} k^{-5/3} f_L(kL) f_\eta(k\eta), \quad (2)$$

116 where the constant  $C \approx 1.5$  is derived from experimental data,  $f_L$  and  $f_\eta$  are non-dimensional  
117 functions. The term  $\varepsilon_{PS}$  should be equal to the TKE dissipation rate  $\varepsilon$  if the second similarity  
118 hypothesis is satisfied.

119 Functions  $f_L$  and  $f_\eta$  specify the shape of energy-spectrum in the energy-containing range and  
 120 the dissipation range respectively.  $L$  is the length scale of large eddies and  $\eta = (\nu^3/\varepsilon)^{1/4}$  is the  
 121 Kolmogorov length scale, which is connected with the dissipative scales. The function  $f_\eta$  tends to  
 122 unity for small  $k\eta$  while  $f_L$  tends to unity for large  $kL$ , such that in the inertial range, the formula  
 123  $E(k) = C\varepsilon_{PS}^{2/3} k^{-5/3}$  is recovered. Pope (2000) proposed the following forms of functions  $f_L$  and  
 124  $f_\eta$

$$f_L(\kappa L) = \left( \frac{\kappa L}{[(\kappa L)^2 + c_L]^{1/2}} \right)^{5/3+p_0}, \quad (3)$$

125 where  $c_L$  is a positive constant,  $p_0 = 2$  and

$$f_\eta(\kappa\eta) = e^{-\beta \{[(k\eta)^4 + c_\eta^4]^{1/4} - c_\eta\}}, \quad (4)$$

126 where  $\beta = 5.2$ ,  $c_\eta = 0.4$ . If  $c_\eta = 0$ , Eq. (4) reduces to the exponential spectrum

$$f_\eta(\kappa\eta) = e^{-\beta k\eta}, \quad (5)$$

127 where  $\beta = 2.1$ . An alternative model spectrum for  $f_\eta$  is the Pao spectrum defined as

$$f_\eta(\kappa\eta) = e^{-\beta(k\eta)^{4/3}}, \quad (6)$$

128 where  $\beta = 2.25$ . One-dimensional longitudinal and transverse energy spectra  $E_{11}$  and  $E_{22}$ , respec-  
 129 tively, are related to the energy spectrum function  $E(k)$  (Pope 2000)

$$E_{11}(k_1) = \int_{k_1}^{\infty} \frac{E(k)}{k} \left( 1 - \frac{k_1^2}{k^2} \right) dk, \quad E_{22}(k_1) = \frac{1}{2} \int_{k_1}^{\infty} \frac{E(k)}{k} \left( 1 + \frac{k_1^2}{k^2} \right) dk. \quad (7)$$

130 In the inertial range, the spectra follow the Kolmogorov's  $-5/3$  law

$$E_{11}(k_1) = \alpha \varepsilon_{PS}^{2/3} k_1^{-5/3}, \quad E_{22}(k_1) = \alpha' \varepsilon_{PS}^{2/3} k_1^{-5/3}, \quad (8)$$

131 where  $\alpha \approx 0.49$  and  $\alpha' \approx 0.65$ . Equations (8) allow to estimate the TKE dissipation rate from the  
 132 inertial-range profile of the one-dimensional energy spectra.



133 Alternatively, the profiles of the second and third order longitudinal structure functions can be  
 134 used to calculate  $\varepsilon$ . The  $n$ -th order structure function reads  $D_n = \langle (u'_l(x+r, t) - u'_l(x, t))^n \rangle$ . Here  
 135  $u'_l$  is the longitudinal component of the velocity fluctuation vector. In the inertial subrange, the  
 136 second and third-order structure functions are related to the dissipation rate by the formulas (e.g.  
 137 Pope (2000))

$$D_2(r) = C_2 \varepsilon_{D_2}^{2/3} r^{2/3}, \quad D_3(r) = -\frac{4}{5} \varepsilon_{D_3} r, \quad (9)$$

138 where  $\varepsilon_{D_2}$  and  $\varepsilon_{D_3}$  should approximate  $\varepsilon$ .

139 In the case of a turbulent signal resolving the smallest scales, the 'direct' relation between the  
 140 TKE dissipation rate and the longitudinal, or transverse, Taylor microscale can be used

$$\varepsilon_\lambda = 15\nu \frac{\langle u_l'^2 \rangle}{\lambda_n^2} = 30\nu \frac{\langle u_l'^2 \rangle}{\lambda_l^2}. \quad (10)$$

141 The longitudinal Taylor microscale equals

$$\lambda_l = \left[ \frac{2\langle u_l'^2 \rangle}{\langle (\partial u'_l / \partial x)^2 \rangle} \right]^{1/2} \quad (11)$$

142 and the transverse microscale is  $\lambda_n = \lambda_l / \sqrt{2}$ . In case of isotropy,  $\varepsilon_\lambda$  coincides with  $\varepsilon$ .

143 Other direct methods for calculating TKE dissipation rate, based on number of zero-crossings,  
 144 have been proposed by Sreenivasan et al. (1983) and are used by many authors, see e.g. Poggi  
 145 and Katul (2009, 2010); Wilson (1995); Yee et al. (1995). The zero-crossings method was first  
 146 introduced by Rice (1945). It assumes that the stochastic process  $q$  and its derivative have Gaussian  
 147 statistics and are statistically independent. Following this, the square of the number of zero-  
 148 crossings per unit time is

$$N^2 = \frac{\langle (\partial q / \partial t)^2 \rangle}{\pi^2 \langle q^2 \rangle}. \quad (12)$$

149 Sreenivasan et al. (1983) considered the Liepmann scale defined as

$$\Lambda = \frac{1}{\pi N_l}, \quad (13)$$

150 where  $N_l$  is a number of zero-crossings of  $u_l'$  per unit length. Using the formula (12) Sreenivasan  
 151 et al. (1983) assumed that  $\Lambda \approx \lambda_n = \lambda_l / \sqrt{2}$ , hence

$$\frac{\lambda_n}{\Lambda} \approx 1. \quad (14)$$

152 For this, it was argued that Eq. (12) also holds for strongly non-Gaussian velocity signals (or for  
 153 non-Gaussian derivative of the time series). This implies that strong departures from Gaussianity  
 154 do not necessarily yield values appreciably different from unity for the ratio of  $\lambda_n / \Lambda$ .

155 Based on this result and Eq. (10), Sreenivasan et al. (1983) proposed a formula for calculating  
 156  $\varepsilon$ , applicable to fully-resolved signals (measured down to the smallest dissipative eddies), which  
 157 reads

$$\varepsilon_{SR} = 15\pi^2 \nu \langle u_l'^2 \rangle N_l^2, \quad (15)$$

158 or for the number of crossings  $N_n$  calculated from the time series of transverse velocity fluctuation  
 159 component  $u_n'$

$$\varepsilon_{SR} = \frac{15}{2} \pi^2 \nu \langle u_n'^2 \rangle N_n^2. \quad (16)$$

160 The number of crossings is related to the energy spectra  $E_{11}$  by the formula

$$\pi^2 \langle u_l'^2 \rangle N_l^2 = \int_0^\infty k^2 E_{11} dk. \quad (17)$$

161 In case a signal is low-pass filtered the number of zero-crossings per unit length depends on cut-  
 162 off wavenumber. Hence, Waławczyk et al. (2017) proposed a possible modification for zero-  
 163 crossing method to retrieve  $\varepsilon$  from the restricted range of  $k$ -values. The motivation was to increase  
 164 robustness of  $\varepsilon$  retrieval using different statistics. Two procedures formulated in Waławczyk et al.  
 165 (2017) are discussed in more detail in subsection 2b, below.

166 *b. Methods based on number of crossings*

167 If we assume that the applied filter is rectangular in the wavenumber space, then from Eqs. (17)  
 168 and (8) the TKE dissipation rate can be estimated from

$$\pi^2 \left( \langle u_1'^2 \rangle N_1^2 - \langle u_i'^2 \rangle N_i^2 \right) = \int_{k_i}^{k_1} k^2 E_{11} dk = \frac{3}{4} \alpha \epsilon_{NC}^{2/3} \left( k_1^{4/3} - k_i^{4/3} \right), \quad (18)$$

169 where  $\langle u_i'^2 \rangle$  is the variance and  $N_i$  is the number of crossings per unit length of a signal filtered  
 170 with a cut-off wavenumber  $k_i$  which is inside the inertial range. Filtering the signal with a series  
 171 of cut-off wavenumbers  $k_i$ ,  $\epsilon_{NC}$  can be estimated from Eq. (18) using a linear least squares fitting  
 172 method, and used as a proxy for the TKE dissipation rate  $\epsilon$ .

173 We note in passing that the scaling of  $N_i$  with  $k_i$  was also investigated by Mazellier and Vassilicos  
 174 (2008) to estimate the dissipation rate constant  $C_\epsilon$  in the Taylor's formula  $\epsilon = C_\epsilon \langle u'^2 \rangle^{3/2} / \mathcal{L}$  where  
 175  $\mathcal{L}$  is the longitudinal integral length scale of turbulence.

176 The second method is based on recovering the missing part of the spectrum in the inertial and  
 177 dissipative range, by introducing a correcting factor to the number of crossings per unit length.  
 178 As such, this method can be treated as a smooth blending between indirect and direct methods as  
 179 it recovers the former as the filter cut-off moves into the inertial range and the latter as the filter  
 180 cut-off moves into the dissipative range.

181 The number of crossings per unit length  $N_{cut}$  is calculated from the low-pass filtered signal,  
 182 where the fine-scale fluctuations have the highest wave number  $k_{cut}$ . Assuming again that the filter  
 183 is rectangular in the wavenumber space, Eq. (17) written for the filtered signal is

$$\pi^2 \langle u_{cut}'^2 \rangle N_{cut}^2 = \int_0^{k_{cut}} k_1^2 E_{11} dk_1, \quad (19)$$

184 where  $\langle u_{cut}'^2 \rangle$  is the variance of the signal. The ratio of Eq. (17) and (19) leads to the formula

$$\langle u_l'^2 \rangle N_l^2 = \langle u_{cut}'^2 \rangle N_{cut}^2 \underbrace{\frac{\int_0^\infty k_1^2 E_{11} dk_1}{\int_0^{k_{cut}} k_1^2 E_{11} dk_1}}_{\mathcal{C}_{\mathcal{F}}} = \langle u_{cut}'^2 \rangle N_{cut}^2 \left( 1 + \frac{\int_{k_{cut}}^\infty k_1^2 E_{11} dk_1}{\int_0^{k_{cut}} k_1^2 E_{11} dk_1} \right), \quad (20)$$

185 where  $\mathcal{C}_{\mathcal{F}}$  is the correcting factor. Assuming the energy spectrum  $E(k)$  can be described by Eq.

186 (2) with  $f_L = 1$  and using relation (7) between  $E(k)$  and  $E_{11}(k_1)$  we obtain

$$E_{11}(k_1) = C \varepsilon^{2/3} \int_{k_1}^\infty k^{-8/3} f_\eta(\beta k \eta) \left( 1 - \frac{k_1^2}{k^2} \right) dk, \quad (21)$$

187 where  $\beta = 2.1$ ,  $C = 1.5$  and  $\eta = (\nu^3/\varepsilon)^{1/4}$  is the Kolmogorov length. Introducing (21) into (20)

188 and changing the variables to  $\xi = \beta k \eta$  and  $\xi_1 = \beta k_1 \eta$ , the correcting factor is obtained as

$$\mathcal{C}_{\mathcal{F}} = 1 + \frac{\int_{k_{cut}}^\infty \beta \eta \xi_1^2 \int_{\xi_1}^\infty \xi^{-8/3} f_\eta(\xi) \left( 1 - \frac{\xi_1^2}{\xi^2} \right) d\xi d\xi_1}{\int_0^{k_{cut}} \beta \eta \xi_1^2 \int_{\xi_1}^\infty \xi^{-8/3} f_\eta(\xi) \left( 1 - \frac{\xi_1^2}{\xi^2} \right) d\xi d\xi_1}. \quad (22)$$

189 With this, the value of dissipation rate can be estimated from Eqs. (15) and (20)

$$\varepsilon_{NCR} = 15\pi^2 \nu \langle u_{cut}'^2 \rangle N_{cut}^2 \mathcal{C}_{\mathcal{F}}. \quad (23)$$

190 In order to calculate  $\mathcal{C}_{\mathcal{F}}$  from Eq. (22) a value of  $\eta$  should first be specified, hence, an iterative

191 procedure was proposed in Waclawczyk et al. (2017). It starts with an initial guess of the TKE

192 dissipation rate,  $\varepsilon^0$ . With this, the corresponding value of the Kolmogorov length  $\eta_0$  is calculated

193 and introduced into Eq. (22) for  $\mathcal{C}_{\mathcal{F}}$ . The TKE dissipation rate after the first iteration,  $\varepsilon^1$  is found

194 from Eq. (23). The procedure can be repeated, i.e. the next approximation of  $\eta^1 = (\nu^3/\varepsilon^1)^{1/4}$  can

195 be calculated and substituted into Eq. (22). After several iterations the procedure converges to the

196 final value of  $\varepsilon_{NCR}$  that should approximate the TKE dissipation rate  $\varepsilon$  with an error defined by a

197 prescribed form  $\Delta\eta = |\eta^{n+1} - \eta^n| < d_\eta$ , where  $d_\eta$  is a given error value.

198 In this method, the cut-off  $k_{cut}$  may be placed in the inertial or dissipative range. In the latter

199 case, the spectral retrieval methods may lead to loss of certain information as they are based on

the inertial-range scaling only. In Waławczyk et al. (2017), performance of the new methods was tested on measurement data obtained during the POST airborne research campaign (Gerber et al. 2013; Malinowski et al. 2013) with the cut-off placed well in the inertial range. It was shown that estimates obtained with the new methods were comparable with results of standard retrieval techniques, however, differing responses to errors due to finite sampling and finite averaging windows were observed. Hence, the new methods can complement the standard techniques to increase robustness of  $\varepsilon$  retrieval.

### c. Alternative formulation of the iterative method

Estimates of  $\varepsilon_{NCR}$  from Eqs. (22) and (23) may be deteriorated if the ratio of the Taylor's microscale to the number of crossings microscale  $\lambda_n/\Lambda$  deviate from unity, see Eq. (14). For this reason, we propose a different formulation of this method.

Based on Eqs. (11, 12, 17) and relation  $\Lambda = \lambda_n = \lambda_l/\sqrt{2}$  we have

$$\frac{1}{4} \left\langle \left( \frac{\partial u'_l}{\partial x} \right)^2 \right\rangle = \int_0^\infty k_1^2 E_{11} dk_1. \quad (24)$$

For low-pass filtered signals (and filters rectangular in the wavenumber space), Eq. (24) becomes

$$\frac{1}{4} \left\langle \left( \frac{\partial u'_{cut}}{\partial x} \right)^2 \right\rangle = \int_0^{k_{cut}} k_1^2 E_{11} dk_1. \quad (25)$$

Hence,  $\langle (\partial u'_{cut}/\partial x)^2 \rangle$  is related to  $\langle (\partial u'_l/\partial x)^2 \rangle$  by the formula

$$\left\langle \left( \frac{\partial u'_l}{\partial x} \right)^2 \right\rangle = \left\langle \left( \frac{\partial u'_{cut}}{\partial x} \right)^2 \right\rangle \frac{\int_0^\infty k_1^2 E_{11} dk_1}{\int_0^{k_{cut}} k_1^2 E_{11} dk_1} = \left\langle \left( \frac{\partial u'_{cut}}{\partial x} \right)^2 \right\rangle \left( 1 + \frac{\int_{k_{cut}}^\infty k_1^2 E_{11} dk_1}{\int_0^{k_{cut}} k_1^2 E_{11} dk_1} \right). \quad (26)$$

If we introduce Eq. (21) for  $E_{11}$  into Eq. (26), we obtain the same correcting factor as in Eq. (22). Based on Eqs. (12), (23) and (26), the value of dissipation rate is

$$\varepsilon_{\lambda R} = 15\nu \left\langle \left( \frac{\partial u'_l}{\partial x} \right)^2 \right\rangle = 15\nu \left\langle \left( \frac{\partial u'_{cut}}{\partial x} \right)^2 \right\rangle_{\mathcal{CF}}. \quad (27)$$

216 An iterative procedure, similar to the one described in subsection 2b will be used to calculate  
 217  $\varepsilon_{\lambda R}$ . With a first guess of  $\varepsilon^0$ , the correcting factor will be calculated from Eq. (22) and introduced  
 218 into Eq. (27) to calculate new value of  $\varepsilon_{\lambda R}$ . The procedure can be continued until the condition  
 219  $\Delta\eta = |\eta^{n+1} - \eta^n| < d_\eta$  is satisfied.

220 In this work, we will investigate and compare the performance of both approaches from  
 221 Waławczyk et al. (2017) and the new Eq. (27) with different model assumptions for  $f_\eta$  as written  
 222 in Eqs. (4) and (6) with DNS. As the DNS data contain complete information about turbulence, it  
 223 will be possible to assess how the  $\varepsilon$  estimates change with changing cut-off wavenumber.

### 224 3. Stratocumulus cloud-top mixing layer simulation for DYCOMS-II RF01 case

225 As a test case, we consider a cloud-top mixing layer. This system mimics the cloud-top region  
 226 of stratocumulus clouds and proves convenient in studying some aspects associated with subme-  
 227 ter scales, like evaporative cooling, as simulations of the complete boundary layer cannot reach  
 228 these small grid spacings (Mellado et al. 2010; Mellado 2017; Mellado et al. 2018). The system  
 229 consists of two horizontal layers of moist air: an upper region, which is warm and unsaturated and  
 230 represents the free troposphere, and a lower region, which is cool and saturated and represents the  
 231 cloud. In-cloud turbulence and the vertical wind shear across the cloud top creates the cloud-top  
 232 mixing layer that is illustrated in Fig. 2. In-cloud turbulence is driven by the longwave radiative  
 233 cooling of the cloud top and by the evaporative cooling caused by the mixing of cloudy and tropo-  
 234 spheric air. Radiative cooling is characterized by the net upward radiative flux  $F_0$  and the radiative  
 235 extinction length  $L_0$ , over which that cooling concentrates. We consider the first research flight  
 236 of the DYCOMS II field campaign as reference, and we use the measurement-based estimates

$L_0 = 15 \text{ m}$  and  $F_0 = 70 \text{ W m}^{-2}$  (Stevens et al. 2003). The radiative properties imply a reference  
 buoyancy flux  $B_0 = F_0 g / (\rho c_p T_0) = 0.002 \text{ m}^2 \text{ s}^{-3}$ , where  $g$  is the gravitational acceleration, and  
 a reference velocity scale  $U_0 = (B_0 L_0)^{1/3} = 0.3 \text{ m s}^{-1}$ . The Reynolds number in the simulation  
 is  $U_0 L_0 / \nu = 800$ , which is about 300 times smaller than that in the atmosphere. The velocity  
 variation across the cloud-top region is  $3 \text{ m s}^{-1}$  (Faloona et al. 2005).

The horizontal size of the computational domain is  $54L_0$ . The domain is discretized with  
 $5120 \times 5120 \times 2048$  points in the streamwise, spanwise and vertical directions, which assures  
 fine resolution of the flow down to the smallest dissipative eddies with a characteristic size  
 $\eta_0 = (\nu^3 / B_0)^{1/3} \simeq 10 \text{ cm}$ . The system is statistically homogeneous over the horizontal planes,  
 the data along these planes are used to construct the different statistics, which depend on the  
 vertical coordinate  $z$  and the time  $t$ . Further details of the simulations can be found in Schulz  
 and Mellado (2018). We investigated the three velocity components in four horizontal planes at  
 heights  $z \in \{-5.2L_0, -3.5L_0, -1.7L_0, 0.1L_0\}$ , where  $z = 0.1L_0$  corresponds to the height of mini-  
 mum buoyancy flux and  $z = -3.5L_0$  corresponds to the height of maximum buoyancy flux.

Figure 3 includes vertical profiles of the mean velocity,  $\langle u \rangle$  in the streamwise ( $x$ ) direction, the  
 root-mean-square (r.m.s.) of the three velocity components  $u_{rms}$ ,  $v_{rms}$  and  $w_{rms}$  in the streamwise,  
 spanwise and vertical directions, respectively and the budget of the turbulence kinetic energy. The  
 angle brackets indicate horizontal average. The viscous dissipation rate of the TKE is defined by  
 equation 1, the buoyancy flux is  $B = \langle b' w' \rangle$ , and the shear production term is  $P = -\langle u' w' \rangle \partial_z \langle u \rangle$ . It  
 is worth to comment that profiles of r.m.s. velocity component fluctuations in figure 3 indicating  
 anisotropy of turbulence are in agreement with the measurement data reported in Jen-La Plante  
 et al. (2016). Moreover, profiles of budget terms of turbulence kinetic energy are consistent with  
 observations reported in Brost et al. (1982) and results of high-resolution large eddy simulations  
 (LES) (Kopeć et al. 2016b; Heinze et al. 2015).

## 4. TKE dissipation rate estimates from inertial-range scaling

### a. DNS signals

The methods related to the local isotropy assumption and inertial-range scaling are commonly used to analyse 1D signals from airborne measurements. At the same time, turbulent flows in clouds or atmospheric boundary layers are in fact inhomogeneous and buoyant. The purpose of this analysis is to check how predictions of these methods, when applied to DNS data, compare with the true value of  $\varepsilon_{DNS}$  calculated from Eq. (1). All analyses were done with MATLAB<sup>®</sup> software.

We first investigated 1D spectra of three velocity components  $u$ ,  $v$  and  $w$ , see Figures 4, 5 and 6, respectively. In order to calculate the compensated spectra, we multiplied each  $E_{11}$ ,  $E_{22}$  and  $E_{33}$  by a corresponding  $\varepsilon_{DNS}^{-2/3}$  at  $z \in \{-5.2L_0, -3.5L_0, -1.7L_0, 0.1L_0\}$  and by  $k_1^{5/3}$  or  $k_2^{5/3}$ . Spectra calculated in  $x$  direction were additionally averaged in the spanwise  $y$  direction. Similarly, spectra calculated in  $y$  direction were averaged in the streamwise  $x$  direction. The horizontal lines in Figures 4, 5 and 6 are equal to the constant coefficients from Eq. (8),  $\alpha = 0.5$  for the longitudinal and  $\alpha' = 0.65$  for the transverse spectra.

We observe similar profiles of corresponding compensated spectra at planes  $z = -5.2L_0$ ,  $-3.5L_0$ ,  $-1.7L_0$ . Results calculated at  $z = 0.1L_0$ , placed in the upper part of stratocumulus cloud, are clearly different. This region of the flow is affected by the presence of shear, stable stratification (see Fig. 3) as well as external intermittency. The contribution of large-scale instabilities induced by the shear is visible in the profile of  $E_{11}(k_1)$  at plane  $z = 0.1L_0$  as a maximum at small  $k$ . Moreover, differences are observed between different types of spectra. The longitudinal ones,  $E_{11}(k_1)$  and  $E_{22}(k_2)$  (Figs. 4a and 5b) seem to closely follow the Kolmogorov's K41 theory in a certain range of wavenumbers. This is in spite of the relatively low- $Re$  number of the considered



284 flow, where a clear separation between the dissipative and energy-containing scales may not be  
 285 attained. At the same time, the transverse spectra  $E_{11}(k_2)$  and  $E_{22}(k_1)$  (Figs. 4b and 5a) seem to  
 286 scale with  $\sim k_1^{-a}$  or  $k_2^{-b}$  where  $a$  and  $b$  are somewhat smaller than  $5/3$ . Interestingly, inertial range  
 287 with the scaling close to  $k_1^{-5/3}$  and  $k_2^{-5/3}$  can be distinguished for the transverse spectra of the third  
 288 velocity component in Fig. 6, however, the constant  $\alpha' \approx 1$  is larger than the value 0.65 at planes  
 289  $z = -5.2L_0, -3.5L_0, -1.7L_0$ . Kaiser and Fedorovich (1998) argued that the excess of  $\alpha'$  over  
 290 value typical for the isotropic turbulence could be caused by the presence of dominating buoyant  
 291 forcing, which favours vertical motions. In such a case, pressure fluctuations were insufficient to  
 292 isotropize turbulence. Spectral anisotropy of velocity component structure in the  $z = 0.1L_0$  layer,  
 293 indicates stable stratification above the cloud top, and is in agreement with the experimental data  
 294 and LES reported in Pedersen et al. (2018).

295 In the following, we investigate to what extent deviations from the K41 theory observed in Figs.  
 296 4-6 affect estimations of  $\varepsilon$ . To estimate  $\varepsilon_{PS}$  from power spectra (Eqs. 8) we fit a line with  $-5/3$   
 297 slope on a logarithmic plot. The log of the intercept is equivalent to  $\alpha\varepsilon_{PS}^{2/3}$  or  $\alpha'\varepsilon_{PS}^{2/3}$ . Figure 7  
 298 provides the scaling of  $N_i^2\langle u_i'^2 \rangle$  with filter cut-off  $k_i$  and  $k_1 = 0.4[m^{-1}]$ , see Eq. (18). For each  $k_i$ , a  
 299 corresponding  $N_i$  of a filtered signal  $u_i'$  was calculated. The linear fit slope is equivalent to  $3\alpha\varepsilon_{NC}^{2/3}$ ,  
 300 out of which the dissipation rate  $\varepsilon_{NC}$  was calculated. We used the sixth order Butterworth filter to  
 301 calculate successive  $u_i'$ , ensuring there was no difference in results between the fifth and the sixth  
 302 order filter, which was also reported in Mazellier and Vassilicos (2008). The frequency response  
 303 characteristic of the filter was investigated in Waławczyk et al. (2017) on artificial velocity time  
 304 series. In this case, the filter led to small (ca. 4%) overprediction of  $\langle u_i'^2 \rangle N_i^2$ . In this work we  
 305 neglected the effect of the filter on  $\varepsilon$  estimates.

Next, we estimate  $\varepsilon_{D_2}$  and  $\varepsilon_{D_3}$  from the second and third order structure functions as written in Eq. (9). We obtained inertial range values by fitting linearly a slope of  $2/3$  to the second order structure function as shown in Fig. 8. Analogous procedure is performed to calculate  $\varepsilon_{D_3}$ .

In isotropic turbulence, all estimates of  $\varepsilon$  should, theoretically, be equal. It would hence seem appropriate to use the same fitting ranges for  $\varepsilon_{PS}$ ,  $\varepsilon_{D_2}$  and  $\varepsilon_{D_3}$ , appropriately converted from  $k$ -space to  $r$ -space (i.e. with  $k = 2\pi/r$ ). In practice, the fitting was difficult due to the short inertial ranges - an attribute of low Reynolds number flows. Although inertial ranges of atmospheric high- $Re$  flows cover a few decades of  $k$  numbers, finite averaging windows and finite resolutions of the measurements cause analogous problems - results are in fact dependent on the chosen fitting ranges. As pointed out in Hou et al. (1998) and confirmed by other authors (Chamecki and Dias 2004), the effect of finite power law range in the spectral space results in a much shorter power law range in the physical space. Also, in our case, the fitting ranges optimal for  $D_2$ , were different than those for power spectra. To show differences in the estimates, we compare results of different methods and different fitting ranges in detail. We consider planes  $z = -3.5L_0$  and  $z = 0.1L_0$ , as they are regions of maximum and minimum buoyancy flux, respectively.

Table 1 presents results for the plane  $z = -3.5L_0$  which is placed in the turbulent region inside the cloud. The true value of  $\varepsilon$  at this plane equals  $\varepsilon_{DNS} = 0.36B_0$ . The first fitting ranges presented in Table 1 seemed to be optimal for the investigated spectra, the second seemed to be optimal for the second-order structure functions  $D_2$ . We present dissipation rate estimates from the power spectrum  $\varepsilon_{PS}$ , number of crossings  $\varepsilon_{NC}$ , second and third order structure functions  $\varepsilon_{D_2}$  and  $\varepsilon_{D_3}$ . We observed a certain discrepancy of results, also between  $\varepsilon_{PS}$  and  $\varepsilon_{D_2}$  that are standard methods of estimating TKE dissipation rate. Moreover,  $\varepsilon_{PS}$  are overpredicted and  $\varepsilon_{D_2}$ ,  $\varepsilon_{D_3}$ ,  $\varepsilon_{NC}$  underpredicted when compared to  $\varepsilon_{DNS} = 0.36B_0$ .

329 The TKE dissipation rate estimates from 1D signals:  $\epsilon_{PS}$ ,  $\epsilon_{D_2}$  and  $\epsilon_{DNS}$  at planes  $z =$   
 330  $-1.7L_0, -3.5L_0, -5.2L_0$  are compared in Fig. 9a. The fitting ranges were chosen to match the  
 331 inertial range of structure functions. It is seen that  $\epsilon_{D_2}$  are in most cases smaller than  $\epsilon_{PS}$ . The  
 332 linear fit for the presented data is

$$\epsilon_{D_2} = 0.96\epsilon_{PS} - 1.2 \times 10^{-4} [m^2/s^3] \quad (28)$$

333 An underprediction of  $\epsilon_{D_2}$  vs.  $\epsilon_{PS}$  was also observed by Jen-La Plante et al. (2016) in the POST  
 334 measurements of stratocumulus clouds in the well-mixed cloud-top layer (therein called CTL).  
 335 Results from POST for this part of the cloud are presented in Fig. 9b and the linear fit is

$$\epsilon_{D_2} = 0.52\epsilon_{PS} + 2.5 \times 10^{-4} [m^2/s^3] \quad (29)$$

336 Having exact DNS data at hand we can observe that the true  $\epsilon_{DNS}$  dissipation rate can differ both  
 337 from  $\epsilon_{D_2}$  and  $\epsilon_{PS}$  (see Fig. 9a). Here, the linear fit line is flat

$$\epsilon_{DNS} = 0.075\epsilon_{PS} + 6.4 \times 10^{-4} [m^2/s^3]. \quad (30)$$

338 Table 2 shows the corresponding fits for the horizontal profile  $z = 0.1L_0$  placed in the upper part  
 339 of the stratocumulus cloud. Here, the discrepancies between  $\epsilon_{DNS}$  and estimates from 1D intersec-  
 340 tions of the velocity field are larger. Results differ also between the horizontal velocity components  
 341 ( $u$  in  $x$ ,  $u$  in  $y$ ,  $v$  in  $x$  and  $v$  in  $y$ ) which makes the local isotropy assumption questionable.

342 As it is seen in Tables 1 and 2, the estimates of  $\epsilon$  from the vertical velocity component  $w$   
 343 differ from those based on horizontal components. They are overpredicted in comparison to  $\epsilon_{DNS}$   
 344 at plane  $z = -3.5L_0$  that is placed inside the CTL, where buoyancy is a source of turbulence  
 345 generation (see Table 1) and greatly underpredicted at plane  $z = 0.1L_0$  (see Table 2) where the  
 346 negative buoyancy damps the vertical velocity fluctuations. In the analysis of POST data by Jen-La  
 347 Plante et al. (2016), the layer of the cloud was referred to as moist and sheared cloud-top mixing

sublayer (CTMSL) and, likewise,  $\varepsilon$  estimates based on  $w$  were underpredicted in this region as compared to estimates from  $u$  (see Fig. 7 therein). In the subsequent sections of this work, we will estimate  $\varepsilon$  based on the 4 signals with horizontal velocity components, in order to obtain results closer to  $\varepsilon_{DNS}$ .

We compare  $\varepsilon$  estimates using the two different fitting ranges from Tables 1 and 2 (averaged over the 4 signals  $u$  in  $x$ ,  $u$  in  $y$ ,  $v$  in  $x$  and  $v$  in  $y$ ) in Figs. 10a and 10b. The structure function's fitting ranges give better results. We can observe that  $\varepsilon_{NC}$  calculated using Eq. (18) agrees closely with  $\varepsilon_{D_2}$  at  $z = -1.7L_0, -3.5L_0, -5.2L_0$ . Our results of  $\varepsilon_{D_3}$  from the third-order function are underestimates (also reported by Chamecki and Dias (2004)), which is contrary to the idea that these estimates are preferable due to their analytically derived constant (4/5). The maximum value of the TKE dissipation rate was found in the cloud-top mixing sublayer  $z = 0.1L_0$ , which agrees with the experiment reported in Jen-La Plante et al. (2016). However, it is seen in 10a that all estimates are underpredicted in comparison to  $\varepsilon_{DNS}$  in this non-isotropic, shear-influenced part of the cloud.

#### *b. Moderate and low-resolution signals*

Signals available from in situ airborne measurements are far from the idealized fully-resolved DNS data. Finite sampling frequency of a sensor and measurement errors induce effective spectral cut-off of velocity time series. In order to investigate the influence of the finite sampling on the TKE dissipation rate estimates, we perform the following tests of DNS data. We consider a virtual aircraft that measures velocity signal with effective cut-off wavenumbers,  $k_{cut} = 0.62, 1.25, 2.5, 5[m^{-1}]$ , placed, approximately, within or close to the inertial range. For each  $k_{cut}$ , if the aircraft flies in the streamwise  $x$  direction we create a new path every 100 grid points in the  $y$  direction, such that 52 signals are collected. Similarly, if the aircraft flies in the  $y$

direction, we create 52 paths in  $x$  direction. In the first test, we average the obtained power spectra and  $\langle u_i'^2 \rangle N_i^2$  profiles and calculate TKE dissipation rates  $\varepsilon_{PS}$  and  $\varepsilon_{NC}$ . Finite sampling frequency cause aliasing i.e. spectral densities for  $k$  higher than the wavenumber  $k_{cut}$  are added to the spectral densities at  $k < k_{cut}$ . This causes a bias error of the TKE dissipation rate estimates. As seen in Fig. 11 the bias of  $\varepsilon_{NC}$  is smaller than the bias of  $\varepsilon_{PS}$ , in particular, results of  $\varepsilon_{NC}$  for  $k_{cut} = 1.25[m^{-1}]$  are still close to  $\varepsilon_{DNS}$ . This result is in line with previous error analyses on artificially generated velocity time series by Waławczyk et al. (2017), where a smaller bias error, however, somewhat larger scatter of  $\varepsilon_{NC}$  was observed in comparison to  $\varepsilon_{PS}$ . In the present analysis, we do not introduce any additional corrections to the power spectra or to the  $\langle u_i'^2 \rangle N_i^2$  profiles, to reduce the bias (such methods can be formulated for high- $Re$  flows, see Sharman et al. (2014)).

Next, in order to test scatter of the results we estimate  $\varepsilon_{PS}$  and  $\varepsilon_{NC}$  from each velocity signal, separately. For a given  $k_{cut}$  we used the same fitting range for all signals. Increasing  $k_{cut}$  we extended the lower bound of the fitting range, that is for  $k_{cut} = 0.62, 1.25, 2.5$  and  $5[m^{-1}]$  the fitting ranges were, respectively,  $k = [0.3m^{-1}, 0.6m^{-1}]$ ,  $k = [0.3m^{-1}, 0.8m^{-1}]$ ,  $k = [0.3m^{-1}, 1.0m^{-1}]$ ,  $k = [0.3m^{-1}, 1.2m^{-1}]$ . Figure 12 presents values of  $\varepsilon_{PS}$  vs.  $\varepsilon_{NC}$  calculated at the plane  $z = -5.2L_0$  for  $k_{cut} = 5[m^{-1}]$  and  $k_{cut} = 0.62[m^{-1}]$ . In Fig. 12a, we observe somewhat larger scatter of  $\varepsilon_{NC}$ , however, as  $k_{cut}$  decreases, scatter of both  $\varepsilon_{NC}$  and  $\varepsilon_{PS}$  becomes comparable, see Fig. 12b.

Additional method enables to decrease statistical uncertainties of the TKE dissipation rate estimates. Figure 13 presents standard errors of  $\varepsilon_{NC}$  and  $\varepsilon_{PS}$ , separately and the error of the mean calculated from a twice larger sample that contains both  $\varepsilon_{NC}$  and  $\varepsilon_{PS}$ . The estimates were done for the  $2 \times 52$  1D intersections (in the  $x$  and  $y$  direction) of the velocity field measured by the virtual aircraft along the plane  $z = -5.2L_0$ . We assume that the samples are uncorrelated, hence the standard error equals  $\sigma = \text{std}(\varepsilon)/\sqrt{N}$ , where  $\text{std}$  is the standard deviation and  $N$  is the size of

the sample. As seen in Fig. 13,  $\sigma_{PS+NC}$ , calculated from the twice larger sample containing both  $\varepsilon_{NC}$  and  $\varepsilon_{PS}$  is smaller than either  $\sigma_{NC}$  or  $\sigma_{PS}$ , individually.

The obtained results confirm the method based on the number of crossings responds differently to errors due to finite sampling, than the spectral retrieval technique. It can also complement standard approaches to reduce the standard error of the mean TKE dissipation rate.

## 5. TKE dissipation rate estimation with the direct and iterative methods

### a. Direct methods

Results discussed in Section 4 reveal TKE dissipation rate recovery based on inertial-range arguments is difficult in the considered flow case. The first source of error relates to the relatively low- $Re$  of DNS simulations. The available DNS data allow the estimation of  $\varepsilon$  from the direct methods. We calculated  $\varepsilon_{SR}$  from the Sreenivasan-Rice formulae Eqs. (15) and (16) (Sreenivasan et al. 1983) and compared it with  $\varepsilon_\lambda$  from Eq. (10). Results for planes  $z = -3.5L_0$  and  $0.1L_0$  are given in Tables 1 and 2. At plane  $z = -3.5L_0$ , the discrepancy between  $\varepsilon_{SR}$  and  $\varepsilon_\lambda$  is caused by the  $\Lambda/\lambda_\eta$  values that deviate from unity. Possible reasons for this could be the low- $Re$  number of the considered flow, and strong non-Gaussianity of the pdfs of velocity derivatives. The estimates of  $\varepsilon_\lambda$  from  $u$  and  $v$  velocity components given in Table 1 are close to  $\varepsilon_{DNS} = 0.36B_0$ , while estimates from the vertical component are overpredicted. This shows, even in the core region of the model cloud the local isotropy assumption is not satisfied.

At the plane  $z = 0.1L_0$  we observe considerable discrepancies between  $\varepsilon_\lambda$  and  $\varepsilon_{SR}$  and large values of  $\Lambda/\lambda_\eta$ , see Table 2. Large  $\Lambda/\lambda_\eta$  were also reported by Kailasnath and Sreenivasan (1993) in the upper part of the boundary layer, affected by the external intermittency. This leads us to the idea that  $\Lambda/\lambda_\eta$  is an indicator of external intermittency, as we will describe in more detail in

416 Section 5c. Values of  $\varepsilon_\lambda$  and  $\varepsilon_{SR}$  averaged over the 4 horizontal signals  $u$  in  $x$ ,  $u$  in  $y$ ,  $v$  in  $x$  and  $v$   
 417 in  $y$  are additionally compared with  $\varepsilon_{DNS}$  in Fig. 14. As before, the largest difference is observed  
 418 at plane  $z = 0.1L_0$  where the given 1D intersections of velocity field are clearly not sufficient to  
 419 estimate the TKE dissipation rate.

#### 420 *b. Two formulations of the iterative method*

421 In this section, we consider the second, iterative approach from Waławczyk et al. (2017), de-  
 422 scribed in Section 2b, where the cut-off can be moved towards dissipative part of the spectrum.  
 423 We test different models for the function  $f_\eta$  in Eq. (22), be it the Pope (4), Pao (6) or the expo-  
 424 nential model (5). Moreover, we discuss results of both formulations of the iterative method, the  
 425 one based on number of crossings (23), as proposed originally in Waławczyk et al. (2017) and  
 426 the new, alternative form based on the variance of velocity derivative, see Eq. (27).

427 Figure 15 presents model spectra of  $u$  in  $x$  for horizontal plane  $z = -3.5L_0$ . As it is seen, the  
 428 Pope formulation (4) provides much better fit with the DNS spectra than the Pao (6) or exponential  
 429 models (5).

430 Next, we investigate DNS signal that is first low-pass filtered with the use of 6<sup>th</sup> order Butter-  
 431 worth filter with a given  $k_{cut}$ . According to the procedure described in Waławczyk et al. (2017), in  
 432 order to estimate  $\varepsilon$  in the iterative method, a first guess for the Kolmogorov length  $\eta = (v^3/\varepsilon)^{1/4}$   
 433 is made. We take  $\varepsilon^0 = \varepsilon_{PS}$ , however, independently of the initial guess the procedure always con-  
 434 verges to the same value of  $\varepsilon_{NCR}$  or  $\varepsilon_{\lambda R}$ . We calculate the correcting factor from Eq. (22) and  
 435 next, the value of dissipation rate is estimated with Eq. (23) or (27). We approximate the integrals  
 436 in Eq. (22) with the trapezoidal rule. We repeat the procedure, as described in Section 2b until  
 437 the condition  $\Delta\eta = |\eta^{n+1} - \eta^n| \leq d_\eta$  with  $d_\eta = 10^{-8}$  is satisfied. Convergence is reached in all  
 438 simulations before the 10th iteration.

Figure 16 shows the difference between  $\varepsilon_{NCR}$  calculated from Eq. (23) and  $\varepsilon_{\lambda R}$  estimated using Eq. (27). The latter compares more favourably with the DNS results over a wide range of  $k_{cut}$  numbers. Again, the best agreement is observed for the Pope model spectrum (4), which is the most favourable choice for the iterative method.

Figure 14 shows  $\varepsilon_{\lambda R}$  and  $\varepsilon_{NCR}$  calculated according to the Pope model for  $k_{cut} = 3[m^{-1}]$ , which is within the dissipative range, as a function of vertical coordinate  $z/L_0$ . Difference in results between both formulations can be explained by the fact that the Rice formula (12) is only approximately satisfied for the considered signals. Let us define the length scale of the filtered signal, analogous to the Taylor microscale (11)  $\lambda_{cut}$

$$\lambda_{cut} = \frac{1}{\sqrt{2}} \left[ \frac{2\langle u_{cut}^2 \rangle}{\langle (\partial u_{cut}' / \partial x)^2 \rangle} \right]^{1/2}. \quad (31)$$

Analogously,  $\Lambda_{cut} = 1/(\pi N_{cut})$  will denote the Liepmann scale calculated for the filtered signal. We note here that in case of the airborne measurements of high- $Re$  turbulence with cut-off wavenumbers placed in the inertial range, investigated in Waćławczyk et al. (2017), the condition  $\Lambda_{cut}/\lambda_{cut} \approx 1$  was satisfied with a good accuracy. As far as the present DNS data are concerned,  $\Lambda_{cut}/\lambda_{cut}$  changes with  $k_{cut}$  (results not shown here). It is closer to 1 if  $k_{cut}$  is placed in the inertial range, however, increases with increasing  $k_{cut}$  towards values presented in Tables 1 and 2. This fact is the source of existing discrepancies between  $\varepsilon_{NCR}$  and  $\varepsilon_{\lambda R}$  and, as seen in Fig. 16b,  $\varepsilon_{\lambda R}$  compares markedly better with  $\varepsilon_{DNS}$ .

### c. $\Lambda/\lambda_n$ ratio as the intermittency measure

The motivation of the present subsection is to understand the reason for the strong deviations of the  $\Lambda/\lambda_n$  ratio from unity. The data seem to suggest that this deviation is caused by the external or global intermittency connected with the existence of laminar spots within the turbulent flow.



460 In the literature, several different methods were proposed to differentiate between rotational  
 461 (turbulent) and irrotational (non-turbulent) parts of a measured velocity signal (Zhang et al. 1996).  
 462 Each requires definition of an indicator function  $q$ , a criterion function  $f(q)$  and a threshold level  
 463  $T_h$ . The flow is assumed turbulent when  $f(q) > T_h$ . If instantaneous values of vorticity  $\omega =$   
 464  $\nabla \times \mathbf{u}$  are known from measurements or DNS data, the enstrophy  $\Omega = 1/2|\omega|^2$  can be used as the  
 465 criterion function  $q$ . However,  $\gamma$  estimation based on vorticity may also be subject to error due to  
 466 presence of mean gradients or non-turbulent wave-like motions that spuriously increase  $\Omega$  above  
 467 the threshold (Ansorge and Mellado 2016).

468 As a first approximation, we assume that in the externally intermittent flow, the statistics will  
 469 change to  $\gamma\langle u'^2 \rangle$  and  $\gamma\langle (\partial u' / \partial x)^2 \rangle$ . Moreover, the laminar part of the signal does not significantly  
 470 contribute to the number of crossings, hence, we will detect  $\gamma N_L$  crossings per unit length in the  
 471 intermittent signal. With this, the Taylor microscale, the Liepmann scale and their ratio will change  
 472 to

$$\lambda_{nI} = \left[ \frac{\gamma\langle u'^2 \rangle}{\gamma\langle (\partial u' / \partial x)^2 \rangle} \right]^{1/2} = \lambda_n, \quad \Lambda_I = \frac{1}{\gamma\pi N_L} = \frac{1}{\gamma}\Lambda, \quad \frac{\lambda_{nI}}{\Lambda_I} = \gamma \frac{\lambda_n}{\Lambda}, \quad (32)$$

473 where the subscripts  $I$  are related to the statistics in the intermittent flow. If  $\lambda_n/\Lambda \approx 1$ , then in the  
 474 intermittent flow,  $\lambda_{nI}/\Lambda_I \approx \gamma$ . We note, however, that in our case  $\lambda_n/\Lambda$  is around 0.8 even in the  
 475 core region of the flow. We will compare predictions of Eq. (32), i.e. the ratio

$$\frac{\lambda_{nI}/\Lambda_I}{(\lambda_n/\Lambda)_T} \quad (33)$$

476 (the subscripts  $T$  is used to denote mean value in the turbulent, core region of the flow) with  $\gamma$ .  
 477 For this purpose, we first subtracted the mean from the instantaneous vorticity. The enstrophy  $\Omega$   
 478 based on the fluctuating vorticity was our criterion function. Regions where  $\Omega$  was smaller than a  
 479 certain threshold value were identified as "laminar spots". We calculated  $\gamma$ , as the mean volume  
 480 fraction of turbulent flow at a given vertical height, by averaging in the streamwise direction and,

481 additionally, in the spanwise direction over four planes  $x/L_0 = 0, 13.5, 27$  and  $40.5$ . In Fig. 17  
 482 this profile is compared with the calculated ratio from Eq. (33). We utilized  $(\lambda_n/\Lambda)_T = 0.83$ .

483 We observe favourable agreement between both curves, at least for larger  $\gamma$  values. Discrepan-  
 484 cies for small  $\gamma$  are due to numerical errors, as both  $\Lambda$  and  $\lambda_n$  are small in these regions. The results  
 485 suggest that the Liepmann-to-Taylor scale ratio, calculated from  $1D$  intersections of velocity field  
 486 is a good indicator of external intermittency. In other words, discrepancies between  $\varepsilon_{NCR}$  and  $\varepsilon_{\lambda R}$   
 487 reported in section 5b reveal the presence of external intermittency in a given flow region.

## 488 6. Conclusions

489 In this work, we focus on scaling of the energy spectra of turbulent flows in stratocumulus  
 490 clouds and investigate different methods of TKE dissipation rate retrieval from  $1D$  intersections of  
 491 the flow domain. We investigate data from numerical experiments in the stratocumulus cloud-top  
 492 mixing layer simulations. In such experiments, high  $Re$  numbers observed in nature could not be  
 493 reached, however, we argue model assumptions can still be tested, enabling conclusions applica-  
 494 ble to 'real-world' flows to be drawn. Finite sampling frequency of a sensor and measurement  
 495 errors deteriorate results of airborne experiments. Comparison with high-resolution numerical  
 496 simulations might help to estimate the role of resulting effective cut-off frequencies and aliasing.

497 The investigated flow case appeared largely influenced by buoyancy effects that cause devia-  
 498 tions from the Kolmogorov scaling. This, in turn, results in errors of the TKE dissipation rate  
 499 retrieval based on local isotropy assumption. We found the longitudinal spectra of horizontal ve-  
 500 locity components  $E_{11}(k_1)$  and  $E_{22}(k_2)$  are comparable to Kolmogorov scaling over certain range  
 501 of wavenumbers, unlike the transverse spectra. The  $1D$  spectra of the vertical component show  
 502  $-5/3$  scaling range; however, the constant  $\alpha'$  is larger than the isotropic value. As a result, TKE  
 503 dissipation rate estimates from  $u$ ,  $v$  and  $w$  velocity components differ, which withstands the local

isotropy assumption. We also show that estimates in the upper section of the cloud are subject to large errors, as the buoyancy flux is minimum and stable stratification strongly hinders vertical motions.

In this work, we investigated different methods of TKE dissipation rate retrieval, including the two approaches based on the number of crossings per length proposed in Waławczyk et al. (2017). The first method used the inertial-range arguments and provided scaling of  $N_i$  in this range. From results presented in Section 4, we can conclude the performance of this approach is comparable with standard spectral retrieval methods. Moreover, we investigated velocity signals with effective spectral cut-off's measured by a "virtual aircraft" flying through the stratocumulus cloud. We showed that  $\varepsilon_{NC}$  estimated from the number of crossings had smaller bias error than  $\varepsilon_{PS}$  calculated from energy spectra. On the other hand, standard deviations of  $\varepsilon_{NC}$  results were larger than that of  $\varepsilon_{PS}$  for 2 higher cut-off's. Still, an additional method of the TKE dissipation rate retrieval allows to reduce standard error of a mean estimated from a finite-size sample.

The second method proposed in Waławczyk et al. (2017) was based on the recovery of the missing part of the spectrum, i.e. the part with  $k$  higher than the cut-off wavenumber  $k_{cut}$ . It is based on a model for the inertial and dissipative parts of the spectrum. Hence, it could be used for signals with  $k_{cut}$  placed in the dissipative range. We showed that Pope's model for the dissipative part of the spectrum provides the best fit to the DNS data. As  $k_{cut}$  moves towards the high-wavenumber part of the spectrum estimated  $\varepsilon_{NCR}$  deteriorated. As identified, the discrepancies follow from the deviations of the Taylor-to-Liepmann scale  $\lambda_n/\Lambda$  from unity. We also showed that this ratio could be used as a certain indicator of the external intermittency.

We proposed an alternative formulation of the second method, where the variance of velocity derivative is used instead of the number of crossings per length. The remaining procedure is consistent, that is, the correction factor for the missing part of the spectrum and  $\varepsilon$  are calcu-

lated iteratively. Results compare very favourably with the DNS data. This also suggests that the dissipative part of the spectrum has a universal form with a prescribed dependence on  $\varepsilon$ .

This study revealed that novel methods for TKE dissipation rate retrieval can complement standard approaches. A perspective for a further study is to test their performance on a larger set of experimental data.

*Acknowledgments.* This work received funding from the European Union Horizon 2020 Research and Innovation Programme under the Marie Skłodowska-Curie Actions, Grant Agreement No. 675675.

MW and SPM acknowledge matching fund from the Polish Ministry of Science and Higher Education No. 341832/PnH/2016. The authors acknowledge the proofreading of the manuscript by Kristin Goździkowska.

## References

- Albertson, J. D., M. B. Parlange, G. Kiely, and W. E. Eichinger, 1997: The average dissipation rate of turbulent kinetic energy in the neutral and unstable atmospheric surface layer. *J. Geophys. Res.*, **102**, 13 423–13 432, doi:<https://doi.org/10.1029/96JD03346>.
- Ansorge, C., and J. P. Mellado, 2016: Analyses of external and global intermittency in the logarithmic layer of Ekman flow. *J. Fluid Mech.*, **805**, 611–635, doi:<https://doi.org/10.1017/jfm.2016.534>.
- Bolgiano, R., 1959: Turbulent spectra in a stably stratified atmosphere. *J. Geophys. Res.*, **64**(12), 2226–2229, doi:<https://doi.org/10.1029/JZ064i012p02226>.
- Brost, R. A., J. C. Wyngaard, and D. H. Lenschow, 1982: Marine stratocumulus layers. part II: Turbulence budgets. *J. Atmos. Sci.*, **39**, 818–836, doi:[https://doi.org/10.1175/1520-0469\(1982](https://doi.org/10.1175/1520-0469(1982)

039(0818:MSLPIT)2.0.CO;2.

Chamecki, M., and N. L. Dias, 2004: The local isotropy hypothesis and the turbulent kinetic energy dissipation rate in the atmospheric surface layer. *Q. J. R. Meteorol. Soc.*, **130**, 2733–2752, doi:<https://doi.org/10.1256/qj.03.155>.

Faloona, I., and Coauthors, 2005: Observations of entrainment in eastern pacific marine stratocumulus using three conserved scalars. *J. Atmos. Sci.*, **62**, 3268–3284, doi:<https://doi.org/10.1256/qj.02.202>.

Gerber, H., G. Frick, S. P. Malinowski, H. Jonsson, D. Khelif, and S. K. Krueger, 2013: Entrainment rates and microphysics in POST stratocumulus. *J. Geophys. Res. Atmos.*, **118**, doi:<https://doi.org/10.1002/jgrd.50878>.

Heinze, R., D. Mironov, and S. Raasch, 2015: Second-moment budgets in cloud topped boundary layers: A large-eddy simulation study. *J. Adv. Model. Earth Syst.*, **7**, 510–536, doi:<https://doi.org/10.1002/2014MS000376>.

Hou, T. Y., X. H. Wu, S. Chen, and Y. Zhou, 1998: Effect of finite computational domain on turbulence scaling in both physical and spectral spaces. *Phys. Rev.*, **E. 58**, 5841–5844, doi:<http://dx.doi.org/10.1103/PhysRevE.58.5841>.

Jen-La Plante, I., and Coauthors, 2016: Physics of stratocumulus top (POST): turbulence characteristics. *Atmos. Chem. Phys.*, **16**, 9711–9725, doi:<https://doi.org/10.5194/acp-16-9711-2016>.

Kailasnath, P., and K. R. Sreenivasan, 1993: Zero crossings of velocity fluctuations in turbulent boundary layers. *Phys. Fluids*, **A 5**, 2879–2885, doi:<https://doi.org/10.1063/1.858697>.

570 Kaiser, R., and E. Fedorovich, 1998: Turbulence spectra and dissipation rates in a wind tunnel  
 571 model of the atmospheric convective boundary layer. *J. Atmos. Sci.*, **55** (4), 580–594, doi:10.  
 572 1175/1520-0469(1998)055<0580:TSADRI>2.0.CO;2.

573 Kimura, Y., and J. R. Herring, 2012: Energy spectra of stably stratified turbulence. *J. Fluid Mech.*,  
 574 **698**, 19–50, doi:10.1017/jfm.2011.546.

575 Kolmogorov, A. N., 1941: Dissipation of energy in locally isotropic turbulence. *Dokl. Akad. Nauk*  
 576 *SSSR*, **434** (1890), 15–17, doi:http://www.jstor.org/stable/51981.

577 Kopeć, J. M., K. Kwiatkowski, S. de Haan, and S. P. Malinowski, 2016a: Retrieving atmospheric  
 578 turbulence information from regular commercial aircraft using Mode-S and ADS-B. *Atmos.*  
 579 *Meas. Tech.*, **9**, 225–2265, doi:https://doi.org/10.5194/amt-9-2253-2016.

580 Kopeć, M. K., S. P. Malinowski, and Z. P. Piotrowski, 2016b: Effects of wind shear and radiative  
 581 cooling on the stratocumulus-topped boundary layer. *Q.J.R. Meteorol. Soc.*, **142**, 3222–3233,  
 582 doi:https://doi:10.1002/qj.2903.

583 Kumar, A., A. G. Chatterjee, and M. K. Verma, 2014: Energy spectrum of buoyancy-driven turbu-  
 584 lence. *Phys. Rev.*, **E 90**, 023 016, doi:10.1103/PhysRevE.90.023016.

585 Kurowski, M. J., S. P. Malinowski, and W. W. Grabowski, 2009: A numerical investigation of  
 586 entrainment and transport within a stratocumulus-topped boundary layer. *Q. J. R. Meteorol.*  
 587 *Soc.*, **135**, 77–92, doi:https://doi.org/10.1002/qj.354.

588 Lindborg, E., 2006: The energy cascade in a strongly stratified fluid. *J. Fluid Mech.*, **550**, 207–242,  
 589 doi:https://doi:10.1017/S0022112005008128.

590 Lumley, J. L., 1964: The spectrum of nearly inertial turbulence in a stably stratified fluid. *J. Atmos.*  
 591 *Sci.*, **21** (1), 99–102, doi:10.1175/1520-0469(1964)021<0099:TSOIT>2.0.CO;2.

592 Malinowski, S. P., and Coauthors, 2013: Physics of stratocumulus top (POST): turbulent mixing  
 593 across capping inversion. *Atmos. Chem. and Phys.*, **13**, 12 171–12 186, doi:[https://doi.org/10.5194/](https://doi.org/10.5194/acp-13-12171-2013)  
 594 acp-13-12171-2013.

595 Mazellier, N., and J. C. Vassilicos, 2008: The turbulence dissipation constant is not universal  
 596 because of its universal dependence on large-scale flow topology. *Phys. Fluids*, **20**, 015 101,  
 597 doi:<https://doi.org/10.1063/1.2832778>.

598 Mellado, J. P., 2017: Cloud-top entrainment in stratocumulus clouds. *Annu. Rev. Fluid Mech.*, **49**,  
 599 145–169, doi:<https://doi.org/10.1146/annurev-fluid-010816-060231>.

600 Mellado, J. P., C. S. Bretherton, B. Stevens, and M. C. Wyant, 2018: DNS and LES for  
 601 simulating stratocumulus: Better together. *J. Adv. Model. Earth Syst.*, **10**, 1421–1438, doi:  
 602 [10.1029/2018MS001312](https://doi.org/10.1029/2018MS001312).

603 Mellado, J. P., B. Stevens, H. Schmidt, and N. Peters, 2010: Two-fluid formulation of the cloud-  
 604 top mixing layer for direct numerical simulation. *Theor. Comput. Fluid Dyn.*, **24**, 511–536,  
 605 doi:[10.1007/s00162-010-0182-x](https://doi.org/10.1007/s00162-010-0182-x).

606 Moeng, C. H., and P. P. Sullivan, 1994: A comparison of shear-driven and bouyancy-driven  
 607 planetary boundary layer flows. *J. Atmos. Sci.*, **51**(7), 999–1022, doi:[https://doi.org/10.1175/](https://doi.org/10.1175/1520-0469(1994)051<0999:ACOSAB>2.0.CO;2)  
 608 1520-0469(1994)051<0999:ACOSAB>2.0.CO;2.

609 Obukhov, A., 1959: Effect of archimedean forces on the structure of the temperature field in a  
 610 turbulent flow. *Dokl. Akad. Nauk SSSR*, **125**, 1246.

611 Patton, E. G., M. J. Judd, and M. R. Raupach, 1998: Large Eddy Simulation of windbreak flow.  
 612 *Bound.-Layer Meteor.*, **87**(2), 275–306, doi:<https://doi.org/10.1023/A:1000945626163>.

613 Pedersen, J. G., Y. Ma, W. W. Grabowski, and S. P. Malinowski, 2018: Anisotropy turbulence and  
614 evolution of marine stratocumulus: Observations and Large Eddy Simulations. *J. Adv. Model.*  
615 *Earth Syst.*, **10**, 500–515, doi:<https://doi.org/10.1002/2017MS001140>.

616 Poggi, D., and G. G. Katul, 2006: Two-dimensional scalar spectra in the deeper layers of a  
617 dense and uniform model canopy. *Bound.-Layer Meteor.*, **121**(2), 267–281, doi:[https://doi.org/](https://doi.org/10.1007/s10546-006-9075-3)  
618 [10.1007/s10546-006-9075-3](https://doi.org/10.1007/s10546-006-9075-3).

619 Poggi, D., and G. G. Katul, 2009: Flume experiments on intermittency and zero-crossing proper-  
620 ties of canopy turbulence. *Phys. Fluids*, **21**, 065 103, doi:<https://doi.org/10.1063/1.3140032>.

621 Poggi, D., and G. G. Katul, 2010: Evaluation of the turbulent kinetic energy dissipation rate inside  
622 canopies by zero- and level-crossing density methods. *Bound.-Layer Meteor.*, **136**, 219–233,  
623 doi:<https://doi.org/10.1007/s10546-010-9503-2>.

624 Pope, S. B., 2000: Turbulent flows. *Cambridge*, doi:<https://doi.org/10.1017/CBO9780511840531>.

625 Rice, S. O., 1945: Mathematical analysis of random noise. *Bell. Syst. Tech. J.*, **24**, 24–156, doi:  
626 [10.1002/j.1538-7305.1945.tb00453.x](https://doi.org/10.1002/j.1538-7305.1945.tb00453.x).

627 Schulz, B., and J. P. Mellado, 2018: Wind shear effects on radiatively and evaporatively  
628 driven stratocumulus tops. *Journal of the Atmospheric Sciences*, **75** (9), 3245–3263, doi:  
629 [10.1175/JAS-D-18-0027.1](https://doi.org/10.1175/JAS-D-18-0027.1).

630 Sharman, R. D., L. B. Cornman, G. Meymaris, J. P. Pearson, and T. Farrar, 2014: Description and  
631 derived climatologies of automated in situ eddy-dissipation-rate reports of atmospheric turbu-  
632 lence. *J. Appl. Meteorol. Clim.*, **53**, 1416–1432, doi:<http://www.jstor.org/stable/51981>.

633 Sreenivasan, K., A. Prabhu, and R. Narasimha, 1983: Zero-crossings in turbulent signals. *J. Fluid*  
634 *Mech.*, **137**, 251–272, doi:<https://doi.org/10.5194/amt-9-2253-2016>.



635 Stevens, B., and Coauthors, 2003: Dynamics and chemistry of marine stratocumulus - DYCOMS-  
 636 II. *Bull. Amer. Meteor. Soc.*, **84** (5), 579–594, doi:10.1175/BAMS-84-5-579.

637 Townsend, A. A., 1956: The structure of turbulent shear flow. *J. Fluid Mech.*, **1** (5), 554–560,  
 638 doi:10.1017/S0022112056210366.

639 Verma, M. K., A. Kumar, and A. Pandey, 2017: Phenomenology of buoyancy-driven turbulence:  
 640 recent results. *New J. Phys.*, **19** (2), 025 012, URL [http://stacks.iop.org/1367-2630/19/i=2/a=](http://stacks.iop.org/1367-2630/19/i=2/a=025012)  
 641 025012.

642 Wacławczyk, M., Y.-F. Ma, J. M. Kopeć, and S. P. Malinowski, 2017: Novel approaches to  
 643 estimating turbulent kinetic energy dissipation rate from low and moderate resolution veloc-  
 644 ity fluctuation time series. *Atmos. Meas. Tech.*, **10**, 4573–4585, doi:[https://doi.org/10.5194/](https://doi.org/10.5194/amt-10-4573-2017)  
 645 amt-10-4573-2017.

646 Waite, M. L., 2011: Stratified turbulence at the buoyancy scale. *Phys. Fluids*, **23**, 066 602, doi:  
 647 <https://doi.org/10.1063/1.3599699>.

648 Wilson, D. J., 1995: *Concentration Fluctuations and Averaging Time in Vapor Clouds*. American  
 649 Institute of Chemical Engineers, New York, doi:10.1002/9780470937976.

650 Yee, E., P. R. Kosteniuk, G. M. Chandler, C. A. Biloft, and J. F. Bowers, 1995: Measurements  
 651 of level-crossing statistics of concentration fluctuations in plumes dispersing in the atmospheric  
 652 surface layer. *Bound.-Layer Meteor.*, **73**, 53–90, doi:<https://doi.org/10.1007/BF00708930>.

653 Zhang, D. H., Y. T. Chew, and S. H. Winoto, 1996: Investigation of intermittency measurement  
 654 methods for transitional boundary layer flows. *Exp. Therm. Fluid Sci.*, **12**, 433–433, doi:<https://doi.org/10.1175/JAS3687.1>.  
 655

## LIST OF TABLES

<b>Table 1.</b>	Values of dissipation rate calculated at horizontal plane $z = -3.5L_0$ , $\epsilon_{PS}$ , $\epsilon_{NC}$ , $\epsilon_{D_2}$ , $\epsilon_{D_3}$ , $\epsilon_{SR}$ and $\epsilon_\lambda$ , are the dissipation rates calculated using Eq. (10), Eq. (8), Eq. (18), Eqs. (9) and Eqs. (15,16), respectively. $\epsilon_{DNS} = 0.36B_0$ is the averaged instantaneous dissipation rate from DNS and $\Lambda/\lambda_\eta$ is the ratio of zero crossing micro-scale to Taylor's micro-scale. The first fitting ranges seemed optimal for power spectra, the second - for structure functions.	33
<b>Table 2.</b>	Values of dissipation rate calculated for horizontal plane $z = 0.1L_0$ , $\epsilon_{PS}$ , $\epsilon_{NC}$ , $\epsilon_{D_2}$ and $\epsilon_{D_3}$ , $\epsilon_{SR}$ , $\epsilon_\lambda$ are the dissipation rates calculated from Eq. (10), Eq. (8), Eq. (18), Eqs. (9) and Eqs. (15,16), respectively. $\epsilon_{DNS} = 0.89B_0$ is the averaged instantaneous dissipation rate from DNS and $\Lambda/\lambda_\eta$ is the ratio of zero crossing micro-scale to Taylor's micro-scale. The first fitting ranges seemed optimal for power spectra, the second - for structure functions.	34

	$k$ - fitting range	$\frac{\varepsilon_{PS}}{B_0}$	$\frac{\varepsilon_{NC}}{B_0}$	$k$ - fitting range	$\frac{\varepsilon_{PS}}{B_0}$	$\frac{\varepsilon_{NC}}{B_0}$	$\frac{\varepsilon_{D_2}}{B_0}$	$\frac{\varepsilon_{D_3}}{B_0}$	$\frac{\varepsilon_{SR}}{B_0}$	$\Lambda/\lambda_n$	$\frac{\varepsilon_\lambda}{B_0}$
$u$ in $x$	0.17 - 0.63	0.47	0.42	0.49 - 0.85	0.41	0.31	0.31	0.23	0.26	1.17	0.37
$v$ in $y$	0.25 - 0.63	0.47	0.40	0.42 - 0.84	0.43	0.33	0.32	0.21	0.26	1.17	0.37
$u$ in $y$	0.29 - 0.84	0.50	0.40	0.84 - 1.67	0.38	0.26	0.30		0.24	1.24	0.37
$v$ in $x$	0.33 - 0.63	0.52	0.41	0.75 - 1.38	0.43	0.29	0.28		0.22	1.24	0.37
$w$ in $x$	0.25 - 0.63	0.65	0.51	0.33 - 0.59	0.63	0.48	0.57		0.27	1.22	0.40
$w$ in $y$	0.17 - 0.63	0.65	0.55	0.33 - 0.59	0.64	0.52	0.58		0.28	1.20	0.40

669 TABLE 1. Values of dissipation rate calculated at horizontal plane  $z = -3.5L_0$ ,  $\varepsilon_{PS}$ ,  $\varepsilon_{NC}$ ,  $\varepsilon_{D_2}$ ,  $\varepsilon_{D_3}$ ,  $\varepsilon_{SR}$  and  
 670  $\varepsilon_\lambda$ , are the dissipation rates calculated using Eq. (10), Eq. (8), Eq. (18), Eqs. (9) and Eqs. (15,16), respectively.  
 671  $\varepsilon_{DNS} = 0.36B_0$  is the averaged instantaneous dissipation rate from DNS and  $\Lambda/\lambda_n$  is the ratio of zero crossing  
 672 micro-scale to Taylor's micro-scale. The first fitting ranges seemed optimal for power spectra, the second - for  
 673 structure functions.

	$k$ - fitting range	$\frac{\varepsilon_{PS}}{B_0}$	$\frac{\varepsilon_{NC}}{B_0}$	$k$ - fitting range	$\frac{\varepsilon_{PS}}{B_0}$	$\frac{\varepsilon_{NC}}{B_0}$	$\frac{\varepsilon_{D_2}}{B_0}$	$\frac{\varepsilon_{D_3}}{B_0}$	$\frac{\varepsilon_{SR}}{B_0}$	$\Lambda/\lambda_n$	$\frac{\varepsilon_\lambda}{B_0}$
$u$ in $x$	0.21 - 0.42	0.91	0.58	0.11 - 0.21	0.93	0.73	1.65	1.20	0.33	1.35	0.64
$v$ in $y$	0.42 - 0.84	0.72	0.63	0.23 - 0.46	0.64	0.37	0.89	0.45	0.45	1.31	0.79
$u$ in $y$	0.42 - 0.84	1.16	0.97	0.71 - 2.09	0.39	0.16	0.25		0.51	1.28	0.84
$v$ in $x$	0.46 - 0.55	0.40	0.33	0.71 - 2.09	0.94	0.87	0.77		0.17	1.46	0.38
$w$ in $x$	0.42 - 0.84	0.37	0.22	0.13 - 0.67	0.23	0.20	0.18		0.16	1.51	0.36
$w$ in $y$	0.84 - 1.64	0.57	0.29	0.80 - 1.33	0.51	0.29	0.27		0.30	1.56	0.73

TABLE 2. Values of dissipation rate calculated for horizontal plane  $z = 0.1L_0$ ,  $\varepsilon_{PS}$ ,  $\varepsilon_{NC}$ ,  $\varepsilon_{D_2}$  and  $\varepsilon_{D_3}$ ,  $\varepsilon_{SR}$ ,  $\varepsilon_\lambda$  are the dissipation rates calculated from Eq. (10), Eq. (8), Eq. (18), Eqs. (9) and Eqs. (15,16), respectively.  $\varepsilon_{DNS} = 0.89B_0$  is the averaged instantaneous dissipation rate from DNS and  $\Lambda/\lambda_n$  is the ratio of zero crossing micro-scale to Taylor's micro-scale. The first fitting ranges seemed optimal for power spectra, the second - for structure functions.

## LIST OF FIGURES

<b>Fig. 1.</b>	Description of zero-crossing approach . . . . .	37
<b>Fig. 2.</b>	Vertical cross section of the liquid water specific humidity in the cloud-top mixing layer. Gray colours indicate regions with $q_\ell$ higher than inside the cloud due to the radiative cooling. The horizontal bars at the sides of the figure indicate the position of the minimum buoyancy flux (horizontal plane $z = 0.1L_0$ , where $L_0$ is the radiative extinction length) and the maximum buoyancy flux (horizontal plane $z = -3.5L_0$ ). . . . .	38
<b>Fig. 3.</b>	Velocity field data in the cloud-top mixing layer. The upper horizontal line indicates the height of minimum buoyancy flux (horizontal plane $z = 0.1L_0$ ) while the lower horizontal black line indicates the height of maximum buoyancy flux (horizontal plane $z = -3.5L_0$ ). . . . .	39
<b>Fig. 4.</b>	Compensated 1D velocity spectra (dimensionless) of the $u$ velocity component at $z \in \{-5.2L_0, -3.5L_0, -1.7L_0, 0.1L_0\}$ a) longitudinal, b) transverse. . . . .	40
<b>Fig. 5.</b>	Compensated 1D velocity spectra (dimensionless) of the $v$ velocity component at $z \in \{-5.2L_0, -3.5L_0, -1.7L_0, 0.1L_0\}$ a) transverse, b) longitudinal. . . . .	41
<b>Fig. 6.</b>	Compensated 1D velocity spectra (dimensionless) of the $w$ velocity component at $z \in \{-5.2L_0, -3.5L_0, -1.7L_0, 0.1L_0\}$ a) transverse in $x$ direction, b) transverse in $y$ direction. . . . .	42
<b>Fig. 7.</b>	Scaling of $u_i'^2 N_i^2$ with filter cut-off $k_i$ calculated at horizontal plane $z = -3.5L_0$ (blue line). The fit is given by a black line. . . . .	43
<b>Fig. 8.</b>	Second- and third- order structure function of $u$ in $x$ at horizontal plane $z = -3.5L_0$ showing the linear fit of a) $\sim r^{2/3}$ , b) $\sim r^1$ . . . . .	44
<b>Fig. 9.</b>	TKE dissipation rates in CTL $\epsilon_{PS}$ vs. $\epsilon_{D_2}$ (red circles) and $\epsilon_{PS}$ vs. $\epsilon_{DNS}$ in the well-mixed cloud-top layer. Solid lines are the linear fit lines. a) stratocumulus cloud-top mixing layer simulation, b) POST measurements (Jen-La Plante et al. 2016). . . . .	45
<b>Fig. 10.</b>	Normalized average TKE dissipation rates calculated from Eq. (8), Eqs. (9) and Eq. (18) as a function of vertical coordinate $z/L_0$ (dimensionless) (a) Fitting ranges were estimated based on $E_{11}$ and $E_{22}$ functions, b) Fitting ranges were estimated based on $D_2$ function. . . . .	46
<b>Fig. 11.</b>	Normalized TKE dissipation rate estimates from signals with effective cut-off's $k_{cut}$ as a function of vertical coordinate $z/L_0$ (dimensionless) a) $\epsilon_{PS}$ , b) $\epsilon_{NC}$ . . . . .	47
<b>Fig. 12.</b>	Profiles of $\epsilon_{NC}$ vs. $\epsilon_{PS}$ normalised with $B_0$ for signals with a) $k_{cut} = 5[m^{-1}]$ b) $k_{cut} = 0.62[m^{-1}]$ . . . . .	48
<b>Fig. 13.</b>	Standard errors of $\epsilon_{NC}$ , $\epsilon_{PS}$ separately and the twice larger sample of $\epsilon_{NC}$ and $\epsilon_{PS}$ normalized with $B_0$ as a function of $k_{cut}$ . Here, $\sigma = \text{std}(\epsilon)/\sqrt{N}$ , where $\text{std}(\epsilon)$ is the standard deviation of TKE dissipation rate estimates and $N$ is the size of the sample. . . . .	49
<b>Fig. 14.</b>	The plot of TKE dissipation rate estimates normalized by $B_0$ as a function of $z/L_0$ (dimensionless), $\epsilon_\lambda$ from Eq. (10), $\epsilon_{SR}$ from Eqs. (15, 16), $\epsilon_{NCR}$ from Eq. (23) and $\epsilon_{\lambda R}$ from Eq. (27). Iterative methods were used with $k_{cut} = 3[m^{-1}]$ . Solid line presents corresponding $\epsilon_{DNS}$ . . . . .	50

716	<b>Fig. 15.</b>	Compensated spectrum of $u$ in $x$ (dimensionless) at $z = -3.5L_0$ as a function of $k_1 \eta$ (dimensionless): black lines - model spectra with dissipative ranges described by Eqs. (4), (6), (5),	
717		blue lines - DNS spectrum . . . . .	51
718			
719	<b>Fig. 16.</b>	The plot of $\varepsilon$ normalized by $B_0$ against different $k_{cut}$ . Results for $u$ in $x$ signal and for plane	
720		$z = -3.5L_0$ . a) method based on the number of crossings and Eq. (23) b) new formulation,	
721		Eq. (27). The straight line represents the value of $\varepsilon_{DNS}$ . . . . .	52
722	<b>Fig. 17.</b>	Values of the intermittency factor calculated from the enstrophy and $\lambda_n/\Lambda$ as a function of	
723		$z/L_0$ (dimensionless). . . . .	53

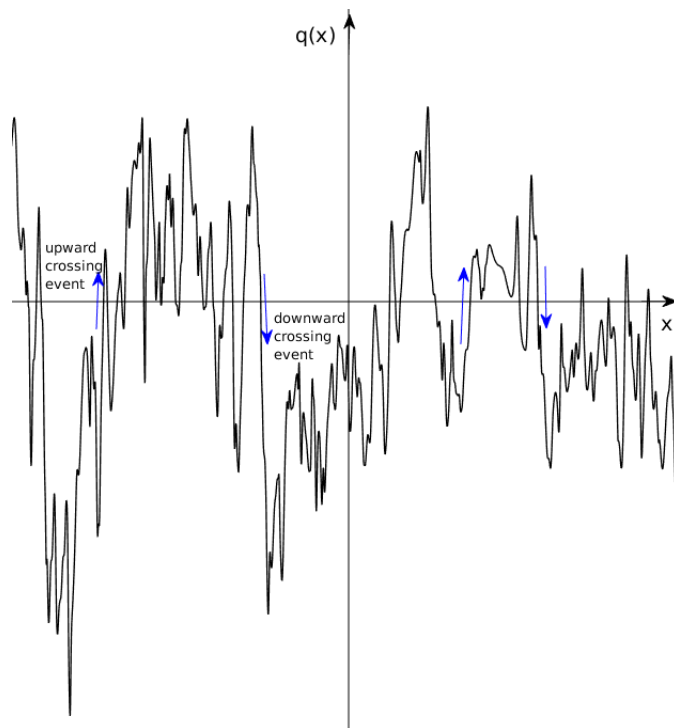


FIG. 1. Description of zero-crossing approach

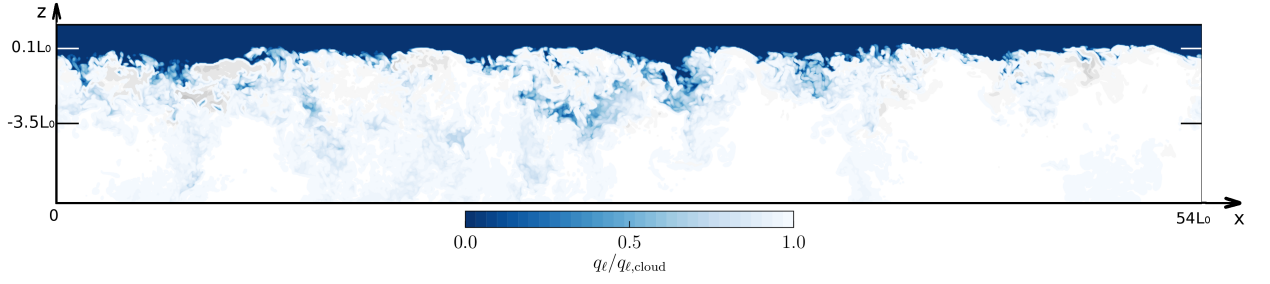


FIG. 2. Vertical cross section of the liquid water specific humidity in the cloud-top mixing layer. Gray colours indicate regions with  $q_\ell$  higher than inside the cloud due to the radiative cooling. The horizontal bars at the sides of the figure indicate the position of the minimum buoyancy flux (horizontal plane  $z = 0.1L_0$ , where  $L_0$  is the radiative extinction length) and the maximum buoyancy flux (horizontal plane  $z = -3.5L_0$ ).



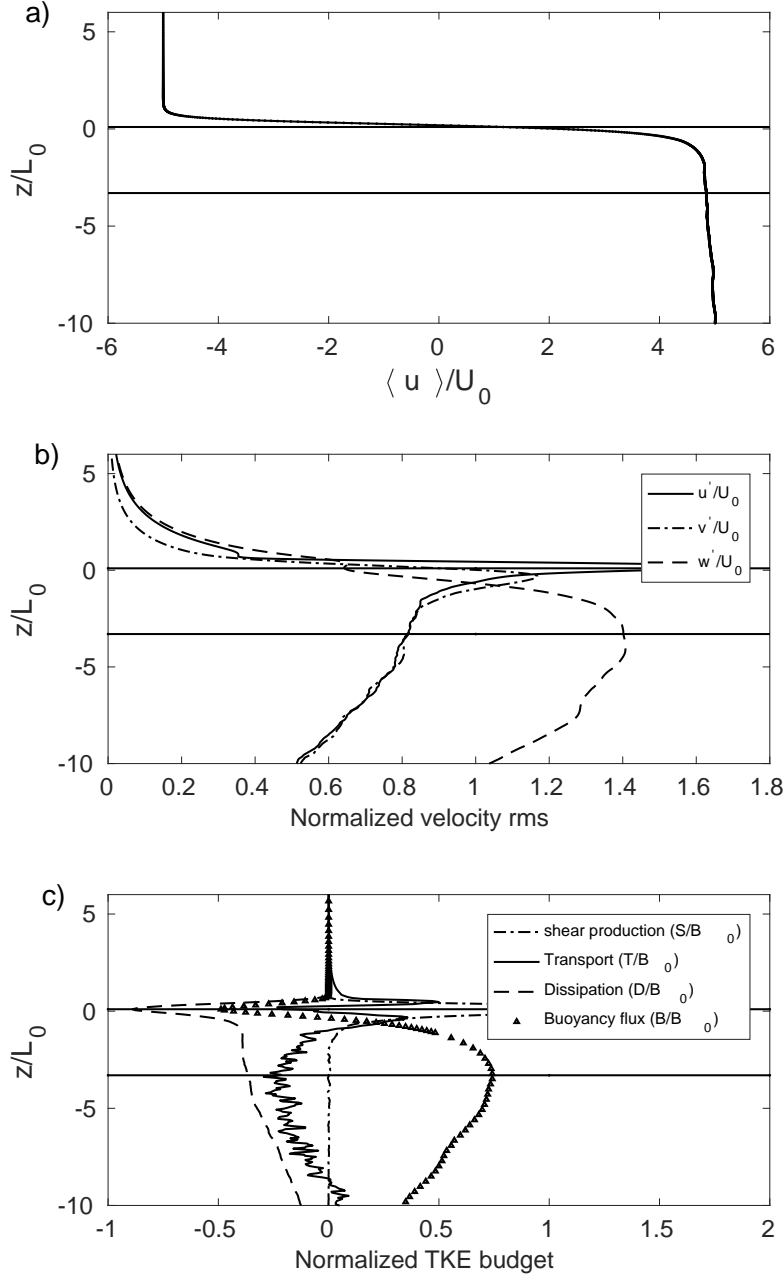


FIG. 3. Velocity field data in the cloud-top mixing layer. The upper horizontal line indicates the height of minimum buoyancy flux (horizontal plane  $z = 0.1L_0$ ) while the lower horizontal black line indicates the height of maximum buoyancy flux (horizontal plane  $z = -3.5L_0$ ).

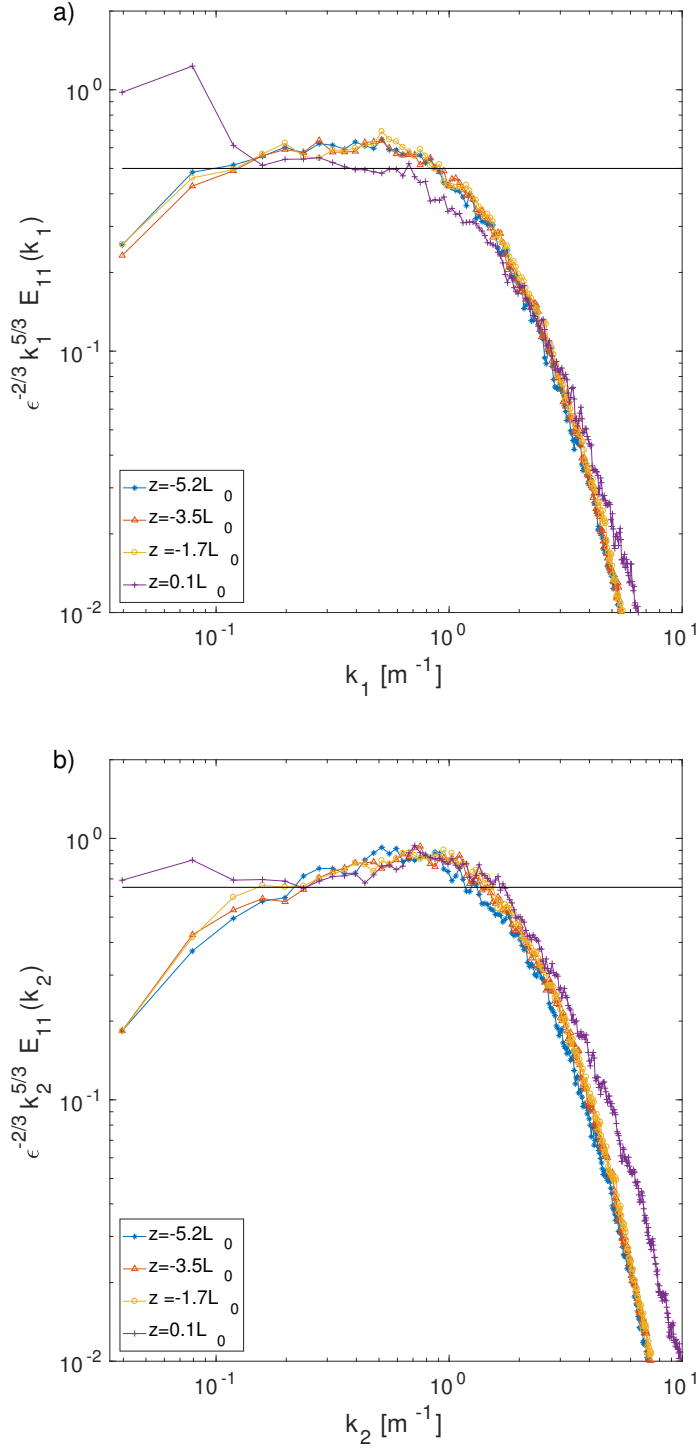


FIG. 4. Compensated 1D velocity spectra (dimensionless) of the  $u$  velocity component at  $z \in \{-5.2L_0, -3.5L_0, -1.7L_0, 0.1L_0\}$  a) longitudinal, b) transverse.

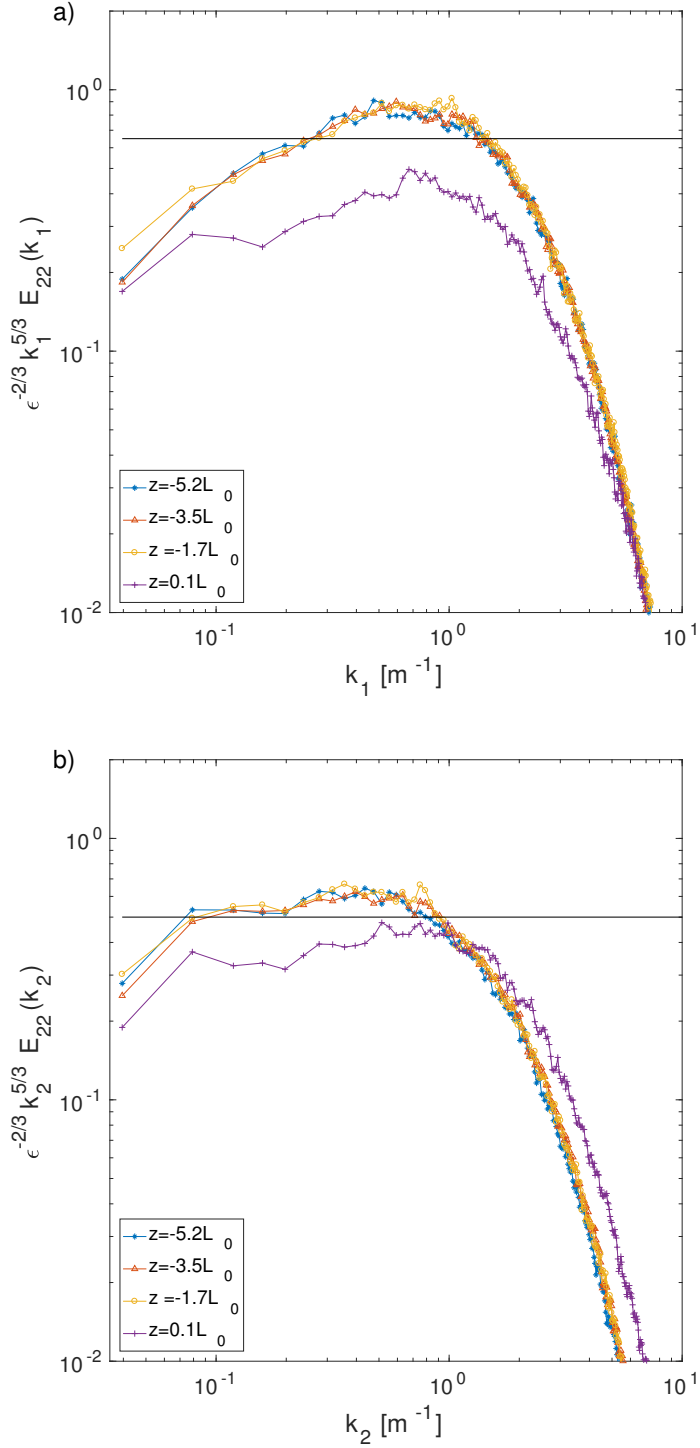


FIG. 5. Compensated 1D velocity spectra (dimensionless) of the  $v$  velocity component at  $z \in \{-5.2L_0, -3.5L_0, -1.7L_0, 0.1L_0\}$  a) transverse, b) longitudinal.

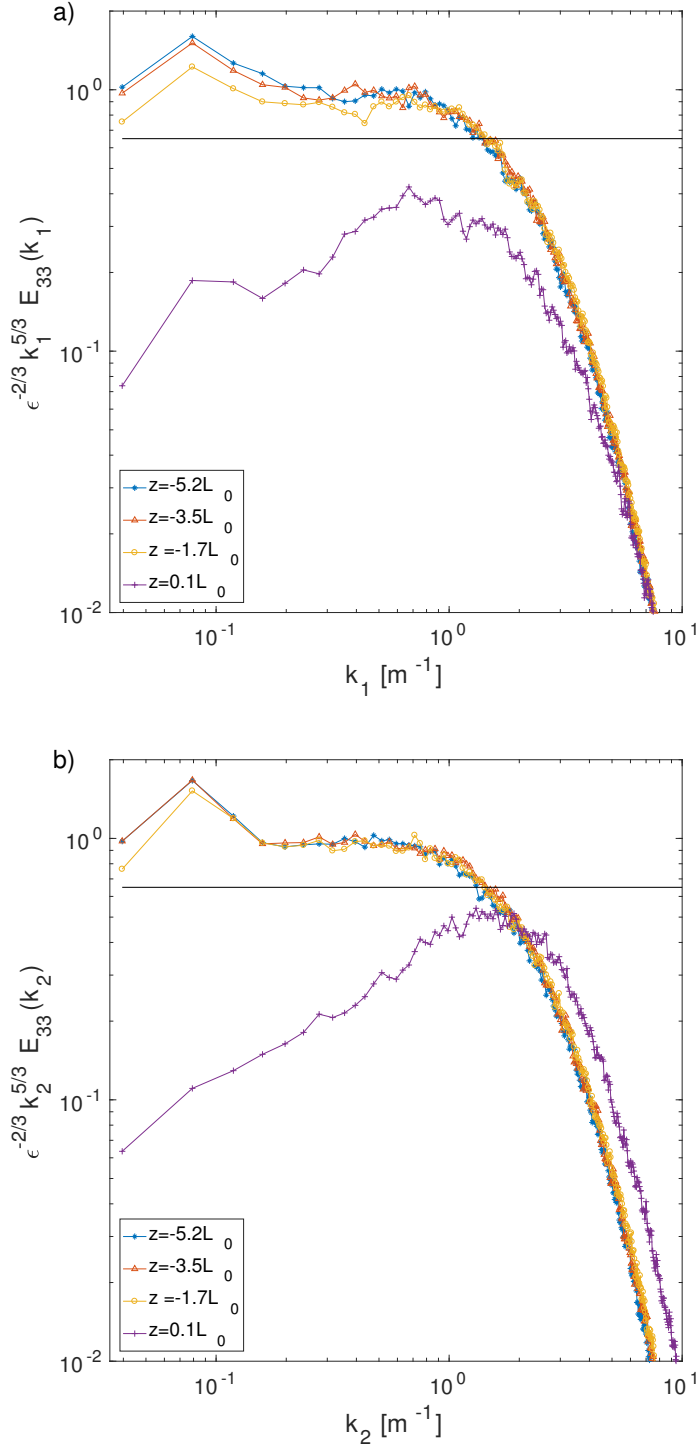


FIG. 6. Compensated 1D velocity spectra (dimensionless) of the  $w$  velocity component at  $z \in \{-5.2L_0, -3.5L_0, -1.7L_0, 0.1L_0\}$  a) transverse in  $x$  direction, b) transverse in  $y$  direction.

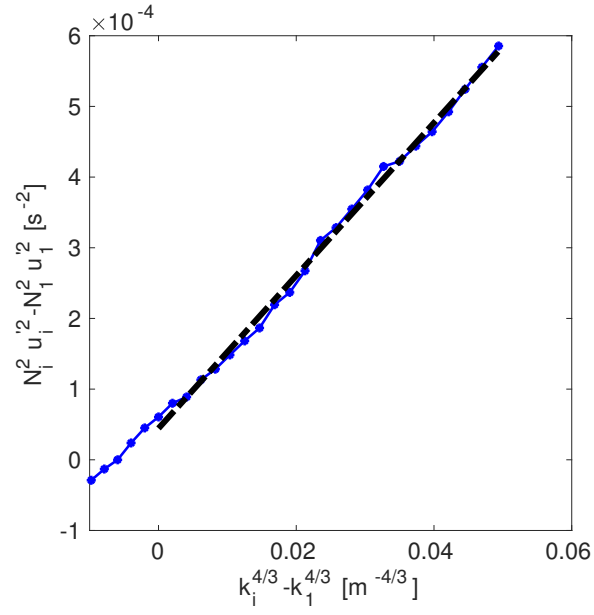


FIG. 7. Scaling of  $u_i'^2 N_i'^2$  with filter cut-off  $k_i$  calculated at horizontal plane  $z = -3.5L_0$  (blue line). The fit is given by a black line.

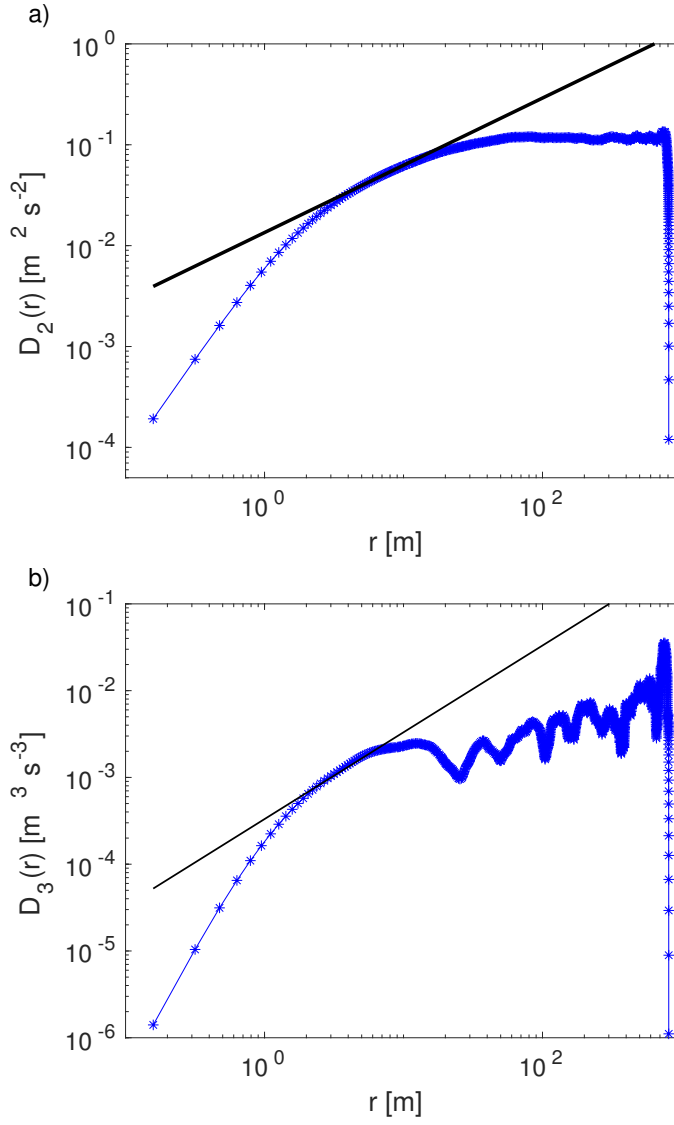


FIG. 8. Second- and third- order structure function of  $u$  in  $x$  at horizontal plane  $z = -3.5L_0$  showing the linear fit of a)  $\sim r^{2/3}$ , b)  $\sim r^1$ .

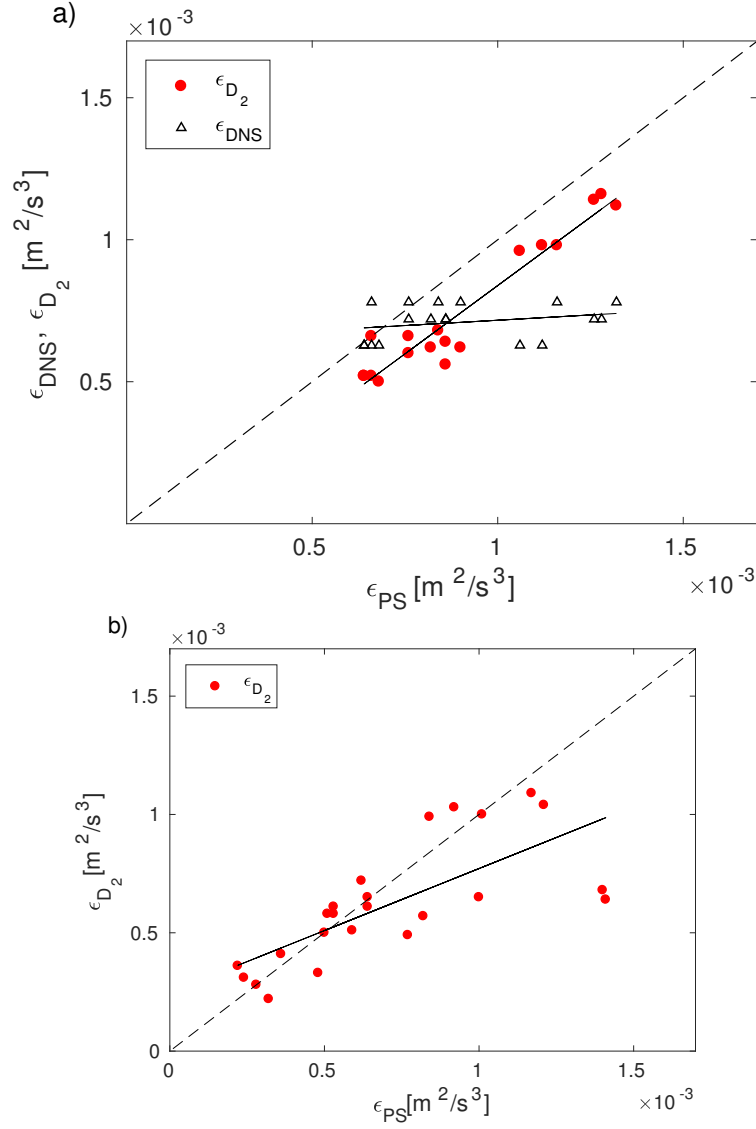


FIG. 9. TKE dissipation rates in CTL  $\epsilon_{PS}$  vs.  $\epsilon_{D_2}$  (red circles) and  $\epsilon_{PS}$  vs.  $\epsilon_{DNS}$  in the well-mixed cloud-top layer. Solid lines are the linear fit lines. a) stratocumulus cloud-top mixing layer simulation, b) POST measurements (Jen-La Plante et al. 2016).

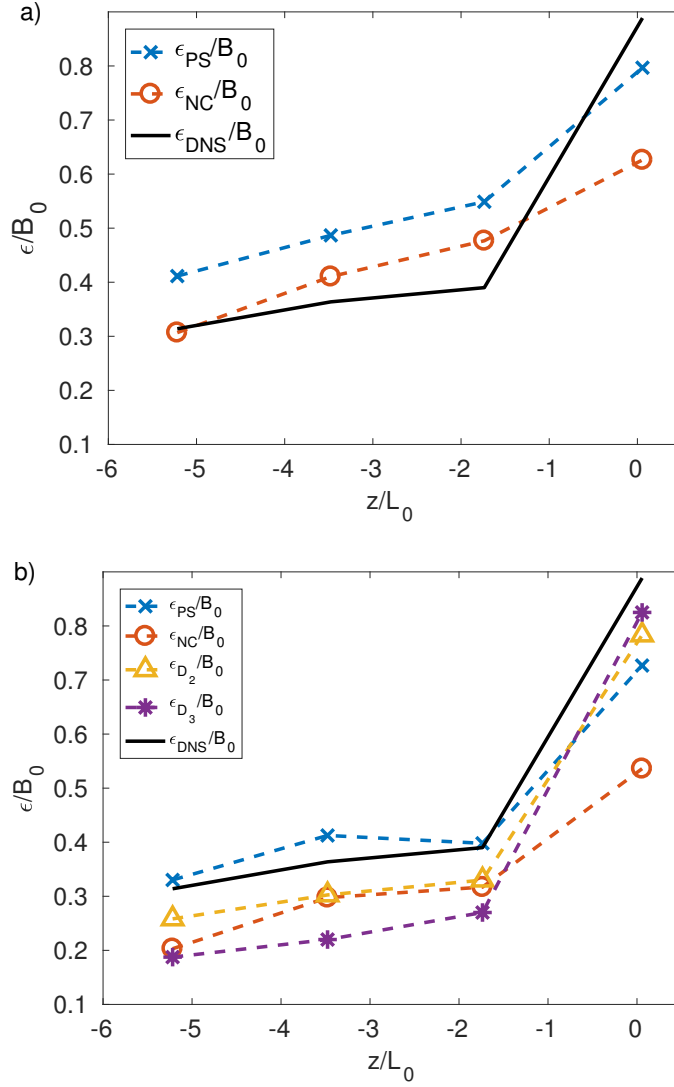


FIG. 10. Normalized average TKE dissipation rates calculated from Eq. (8), Eqs. (9) and Eq. (18) as a function of vertical coordinate  $z/L_0$  (dimensionless) (a) Fitting ranges were estimated based on  $E_{11}$  and  $E_{22}$  functions, b) Fitting ranges were estimated based on  $D_2$  function.



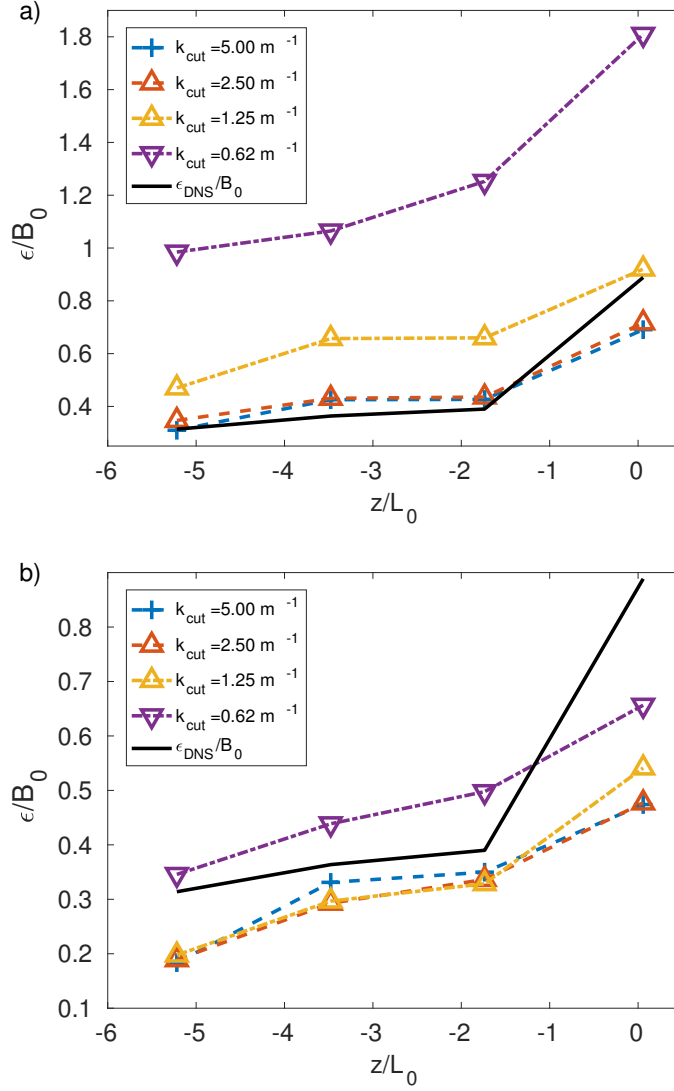


FIG. 11. Normalized TKE dissipation rate estimates from signals with effective cut-off's  $k_{\text{cut}}$  as a function of vertical coordinate  $z/L_0$  (dimensionless) a)  $\epsilon_{PS}$ , b)  $\epsilon_{NC}$ .

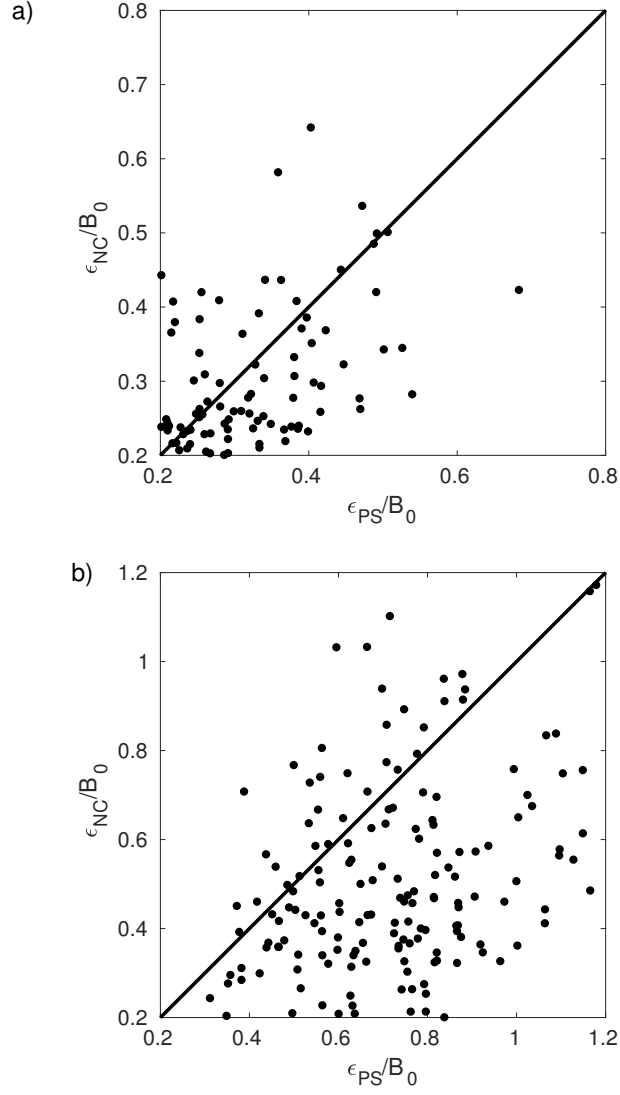


FIG. 12. Profiles of  $\epsilon_{NC}$  vs.  $\epsilon_{PS}$  normalised with  $B_0$  for signals with a)  $k_{cut} = 5[m^{-1}]$  b)  $k_{cut} = 0.62[m^{-1}]$ .

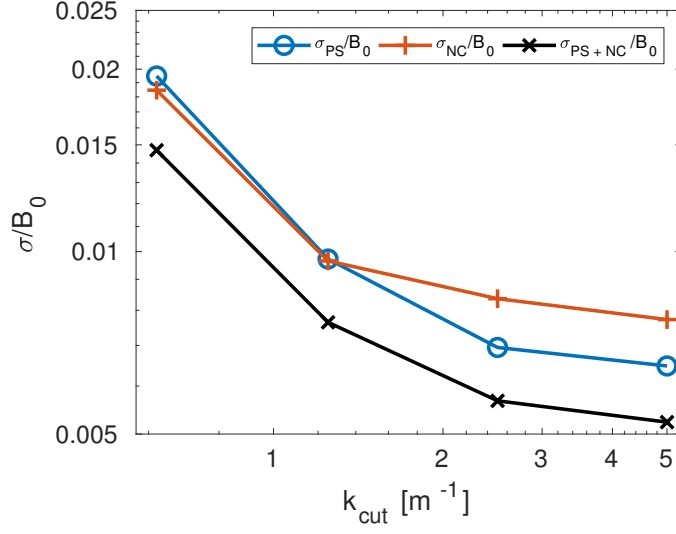


FIG. 13. Standard errors of  $\varepsilon_{\text{NC}}$ ,  $\varepsilon_{\text{PS}}$  separately and the twice larger sample of  $\varepsilon_{\text{NC}}$  and  $\varepsilon_{\text{PS}}$  normalized with  $B_0$  as a function of  $k_{\text{cut}}$ . Here,  $\sigma = \text{std}(\varepsilon)/\sqrt{N}$ , where  $\text{std}(\varepsilon)$  is the standard deviation of TKE dissipation rate estimates and  $N$  is the size of the sample.

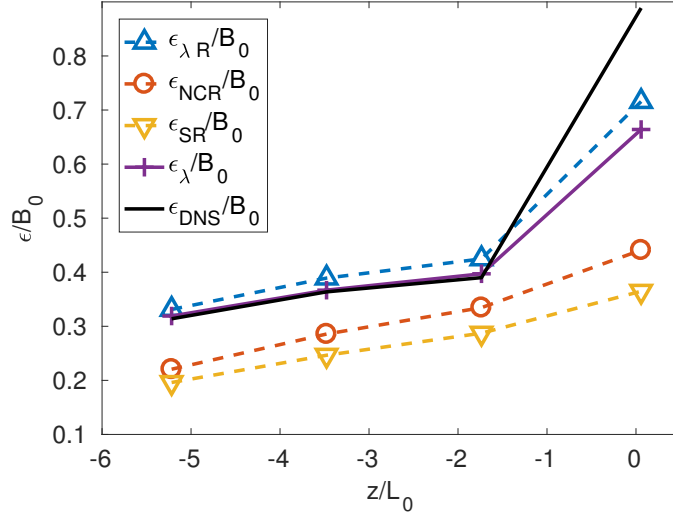


FIG. 14. The plot of TKE dissipation rate estimates normalized by  $B_0$  as a function of  $z/L_0$  (dimensionless),  $\epsilon_{\lambda}$  from Eq. (10),  $\epsilon_{SR}$  from Eqs. (15, 16),  $\epsilon_{NCR}$  from Eq. (23) and  $\epsilon_{\lambda R}$  from Eq. (27). Iterative methods were used with  $k_{cut} = 3[m^{-1}]$ . Solid line presents corresponding  $\epsilon_{DNS}$ .

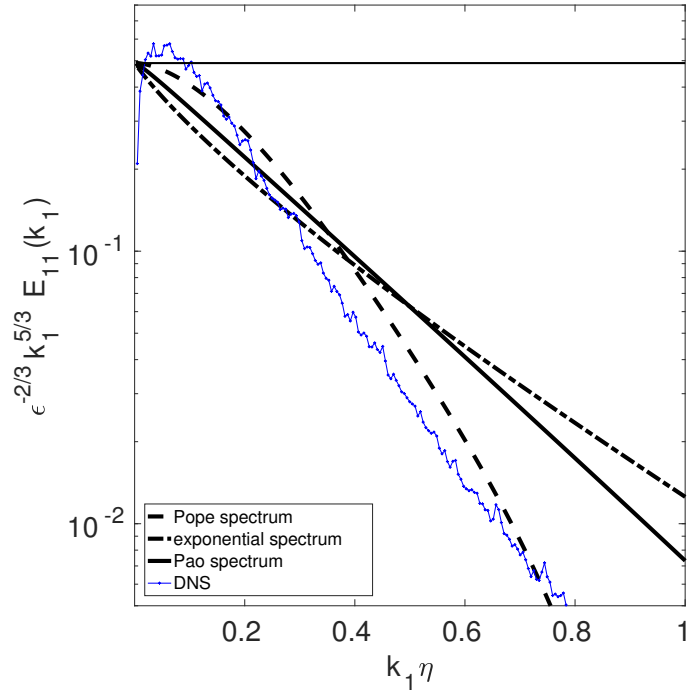


FIG. 15. Compensated spectrum of  $u$  in  $x$  (dimensionless) at  $z = -3.5L_0$  as a function of  $k_1 \eta$  (dimensionless):

black lines - model spectra with dissipative ranges described by Eqs. (4), (6), (5), blue lines - DNS spectrum

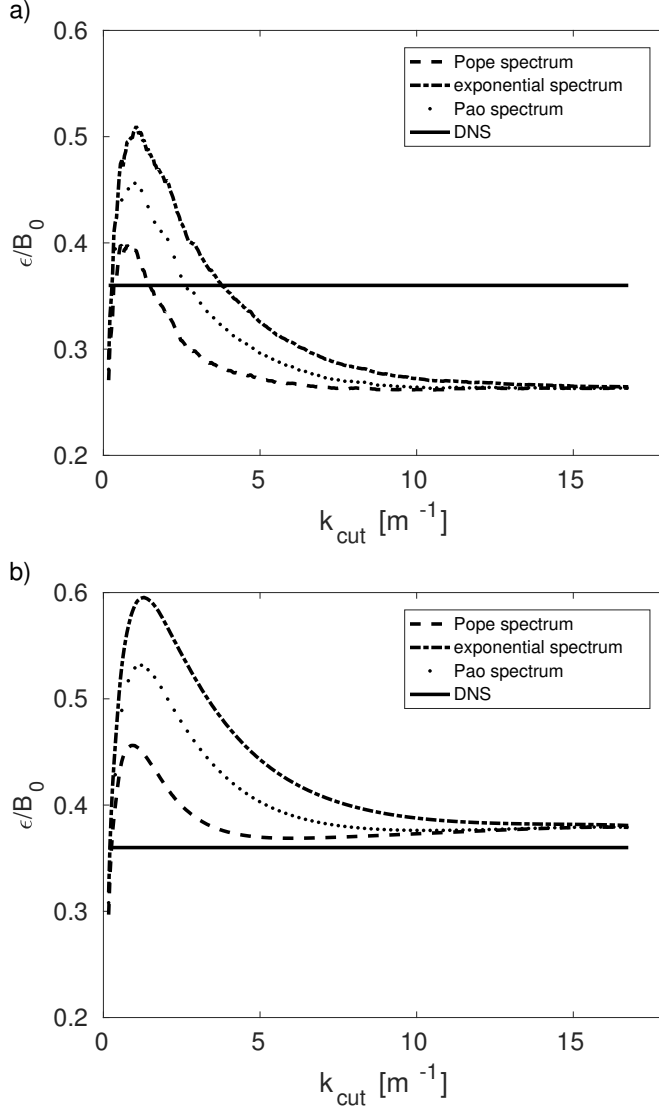


FIG. 16. The plot of  $\epsilon$  normalized by  $B_0$  against different  $k_{cut}$ . Results for  $u$  in  $x$  signal and for plane  $z = -3.5L_0$ . a) method based on the number of crossings and Eq. (23) b) new formulation, Eq. (27). The straight line represents the value of  $\epsilon_{DNS}$ .

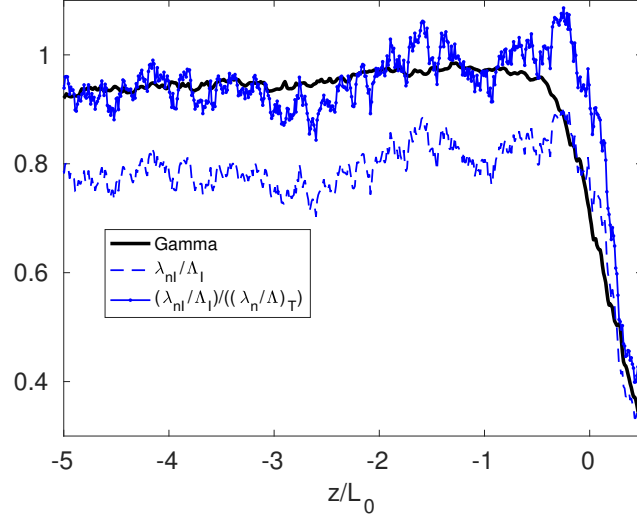


FIG. 17. Values of the intermittency factor calculated from the enstrophy and  $\lambda_n/\Lambda$  as a function of  $z/L_0$  (dimensionless).